Resident Kupffer cells and neutrophils drive liver toxicity in cancer immunotherapy

Siwicki, Marie; Gort-Freitas, Nicolas A; Messemaker, Marius; Bill, Ruben; Gungabeesoon, Jeremy; Engblom, Camilla; Zilionis, Rapolas; Garris, Christopher; Gerhard, Genevieve M; Kohl, Anna; Lin, Yunkang; Zou, Angela E; Cianciaruso, Chiara; Bolli, Evangelia [**and 22 more**]

How to cite

SIWICKI, Marie et al. Resident Kupffer cells and neutrophils drive liver toxicity in cancer immunotherapy. In: Science Immunology, 2021, vol. 6, n° 61, p. eabi7083. doi: 10.1126/sciimmunol.abi7083

This publication URL: https://archive-ouverte.unige.ch/unige:152850

Publication DOI: 10.1126/sciimmunol.abi7083

CANCER IMMUNOLOGY

Resident Kupffer cells and neutrophils drive liver toxicity in cancer immunotherapy

**Marie Siwicki[1], Nicolas A. Gort-Freitas[2], Marius Messemaker[1], Ruben Bill[1], Jeremy Gungabeesoon[1], Camilla Engblom[1], Rapolas Zilionis[2,3], Christopher Garris[1], Genevieve M. Gerhard[1], Anna Kohl[1], Yunkang Lin[1], Angela E. Zou[1], Chiara Cianciaruso[1,4], Evangelia Bolli[1,4], Christina Pfirschke[1], Yi-Jang Lin[1], Cecile Piot[1], John E. Mindur[1], Nilesh Talele[5], Rainer H. Kohler[1], Yoshiko Iwamoto[1], Mari Mino-Kenudson[6], Sara I. Pai[7], Claudio deVito[4,8], Thibaud Koessler[9,10,11], Doron Merkler[4,8], Alexander Coukos[12], Alexandre Wicky[12], Montserrat Fraga[13,14], Christine Sempoux[15], Rakesh K. Jain[5], Pierre-Yves Dietrich[9,10,11], Olivier Michielin[12], Ralph Weissleder[1,2], Allon M. Klein[2], Mikael J. Pittet[1,4,9,10,11]*

Immunotherapy is revolutionizing cancer treatment but is often restricted by toxicities. What distinguishes adverse events from concomitant antitumor reactions is poorly understood. Here, using anti-CD40 treatment in mice as a model of T_H1-promoting immunotherapy, we showed that liver macrophages promoted local immune-related adverse events. Mechanistically, tissue-resident Kupffer cells mediated liver toxicity by sensing lymphocyte-derived IFN-γ and subsequently producing IL-12. Conversely, dendritic cells were dispensable for toxicity but drove tumor control. IL-12 and IFN-γ were not toxic themselves but prompted a neutrophil response that determined the severity of tissue damage. We observed activation of similar inflammatory pathways after anti–PD-1 and anti–CTLA-4 immunotherapies in mice and humans. These findings implicated macrophages and neutrophils as mediators and effectors of aberrant inflammation in T_H1-promoting immunotherapy, suggesting distinct mechanisms of toxicity and antitumor immunity.

INTRODUCTION

Patients receiving immunotherapy for cancer can experience immune-related adverse events (irAEs) in normal, noncancerous tissue, which frequently leads to discontinuation or disruption of therapy (*1*, *2*). Toxicity appears to correlate with antitumor efficacy (*3*, *4*); yet, whether similar or different mechanisms drive antitumor immunity and irAEs is largely unknown.

Interferon-γ (IFN-γ) and interleukin-12 (IL-12) induction accompany effective antitumor immune responses, both in mice (*5*–*8*) and humans (*9*–*11*). These cytokines are characteristic of cell-mediated, T helper 1 (T_H1)–polarized immunity and are appreciated as important in the body's response to cancer. Myeloid cell–targeted and lymphocyte-targeted therapies can similarly promote both cytokines (*7*), and their induction is crucial in the rational design of cancer immunotherapeutics. However, robust activation of IFN-γ and IL-12 can be toxic in both humans and mice (*12*–*15*), suggesting that these cytokines may be involved with both productive antitumor immunotherapy responses and irAEs.

To understand how the canonical antitumoral cytokines IL-12 and IFN-γ might detrimentally affect tumor-free tissues in the setting of immunotherapy, we used the T_H1-activating myeloid cell agonist anti-CD40 (aCD40). Similar to checkpoint inhibitors, aCD40 causes a T_H1-polarized antitumor response; however, whereas mice tolerated checkpoint inhibitors in tumor-free tissues, aCD40 caused systemic immune activation and multiorgan toxicities. Therefore, we used aCD40 as a tool to robustly induce IL-12– and IFN-γ–dependent responses in tumor-bearing mice and to interrogate whether some features of the T_H1 response could distinguish antitumor immunity from undesired therapy-driven pathology. Understanding mechanisms of toxicities associated with aCD40 treatment is of clinical interest in its own right because CD40 agonists are potentially powerful to treat cancer but can trigger adverse events in patients (*16*). Although we found that aCD40 triggered an inflammatory response in various tissue sites, we predominantly focused on the liver to interrogate mechanisms governing toxicity because this is a clinically important site of irAEs. We further tested whether immune checkpoint blockers, anti-programmed cell death protein 1 (anti–PD-1) and anti-cytotoxic T-lymphocyte–associated protein 4 (anti–CTLA-4), could trigger similar inflammatory pathways in mice and humans.

RESULTS

aCD40 triggered proinflammatory T_H1 cytokines throughout a tumor-bearing host

To study T_H1 cytokine responses in tumor-free tissues, we initially analyzed multiple organs throughout IL-12p40 and IFN-γ reporter mice bearing MC38 flank tumors, comparing untreated mice to

[1]Center for Systems Biology, Massachusetts General Hospital Research Institute and Harvard Medical School, Boston, MA, USA. [2]Department of Systems Biology, Harvard Medical School, Boston, MA, USA. [3]Institute of Biotechnology, Life Sciences Center, Vilnius University, Vilnius, Lithuania. [4]Department of Pathology and Immunology, University of Geneva, Geneva, Switzerland. [5]Edwin L. Steele Laboratories, Department of Radiation Oncology, Massachusetts General Hospital, Harvard Medical School, Boston, MA, USA. [6]Department of Pathology, Massachusetts General Hospital, Boston, MA, USA. [7]Department of Surgery, Massachusetts General Hospital, Harvard Medical School, Boston, MA, USA. [8]Division of Clinical Pathology, Geneva University Hospital, Geneva, Switzerland. [9]Department of Oncology, Geneva University Hospitals, Geneva, Switzerland. [10]Center for Translational Research in Onco-Hematology, University of Geneva, Geneva, Switzerland. [11]Swiss Cancer Center Leman (SCCL), Lausanne and Geneva, Switzerland. [12]Precision Oncology Center, Department of Oncology, Lausanne University Hospital CHUV, Lausanne, Switzerland. [13]Faculty of Biology and Medicine, University of Lausanne, Lausanne, Switzerland. [14]Service of Gastroenterology and Hepatology, Lausanne University Hospital, Lausanne, Switzerland. [15]Institute of Pathology, University Hospital and University of Lausanne, Lausanne, Switzerland.
*Corresponding author. Email: mikael.pittet@unige.ch

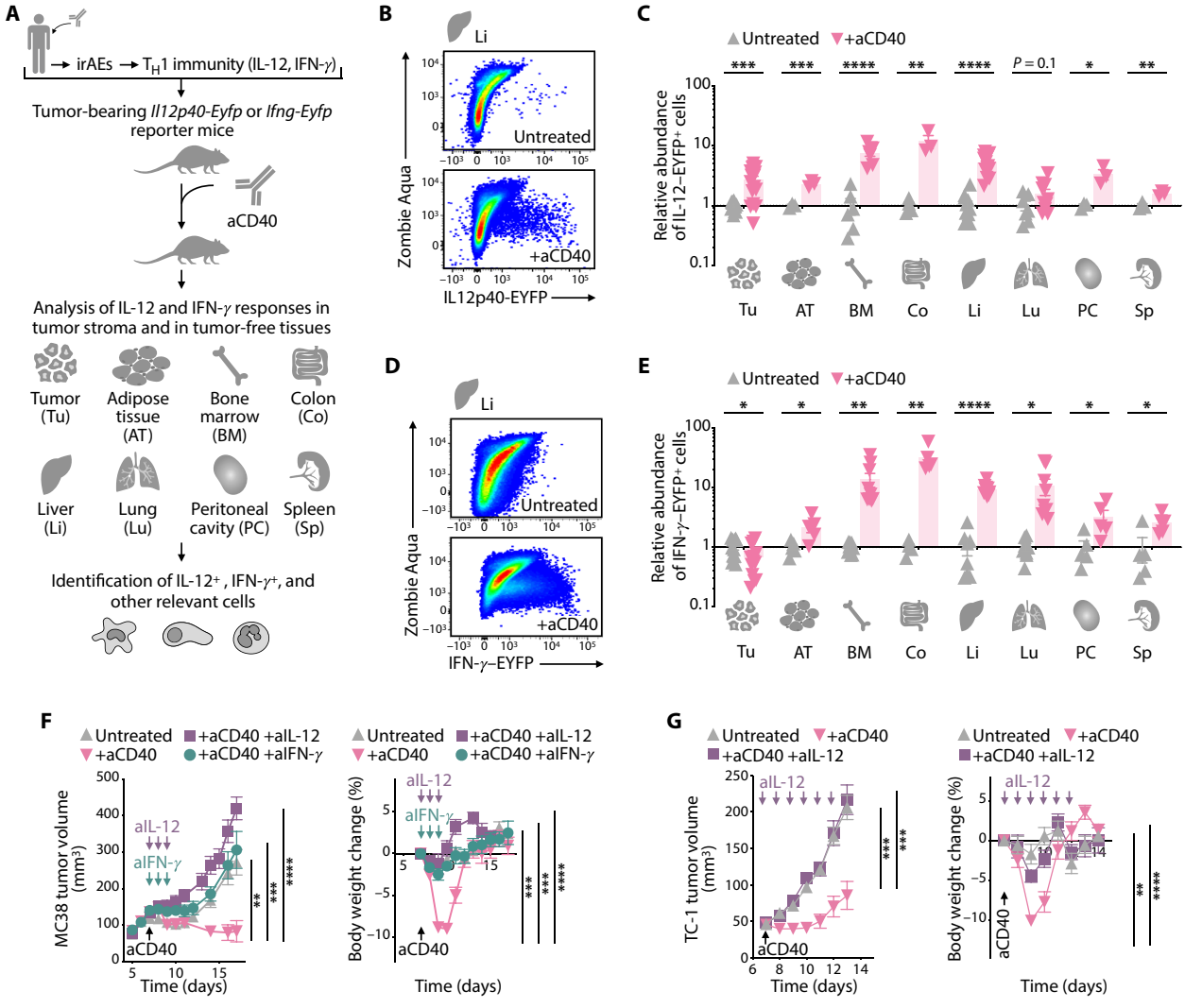

Fig. 1. aCD40 triggered canonical antitumor T_H1 cytokines throughout a tumor-bearing host. (**A**) Rationale and workflow to study of irAEs using IL-12 and IFN-γ reporter mice. (**B**) Flow cytometry plots exemplifying IL-12p40–EYFP induction in liver on day 2 after aCD40. *y* axis, viability dye (Zombie Aqua). (**C**) IL-12p40–EYFP induction across tissues on day 2 after aCD40. Values calculated on the basis of percentage of $CD45^+$ events that are $EYFP^+$ ($n = 3$ to 16 mice per group). (**D**) Flow cytometry plots exemplifying IFN-γ–EYFP induction in liver on day 2 after aCD40 treatment. *y* axis as in (B). (**E**) IFN-γ–EYFP induction across tissues on day 2 after aCD40. Values calculated as in (C) ($n = 5$ to 14 mice per group). (**F**) MC38 tumor volumes and changes in body weight for mice treated or not with aCD40 with or without IL-12 or IFN-γ neutralization ($n = 5$ to 7 mice per group). (**G**) TC-1 tumor volumes and changes in body weight for mice treated or not with aCD40 with or without IL-12 neutralization ($n = 7$ to 9 mice per group). Data are represented as means ± SEM. For comparisons between two groups, Student's two-tailed *t* test was used. For comparisons between multiple groups, one-way ANOVA was used. $^*P < 0.05$; $^{**}P < 0.01$; $^{***}P < 0.001$; $^{****}P < 0.0001$.

those receiving aCD40 (Fig. 1A). We chose MC38 tumors because they can be controlled by systemically delivered T_H1-inducing immunotherapies (*7*, *17*), and we have previously shown that aCD40 stimulates a robust T_H1 immune response associated with MC38 tumor control (*7*). aCD40 elevated both IL-12p40 and IFN-γ in nearly all tissues analyzed (Fig. 1, B to E, and fig. S1, A and B). As an exception, we could not detect an IFN-γ response at the tumor site by flow cytometry, although this response has been documented when using a less invasive approach such as intravital microscopy (*7*).

Mice experience weight loss in the days after aCD40 therapy (*14*, *18*), which we initially used as a proxy for systemic toxicity. Cytokine neutralization showed that MC38 tumor control and weight loss both depended on IL-12p40 and IFN-γ (Fig. 1F). Neutralizing IL-12p40 similarly diminished tumor control and weight loss after aCD40 in TC-1 tumor-bearing mice (Fig. 1G). Toxicity did not depend on IL-23, which uses IL-12p40 in its heterodimeric structure (fig. S2). These findings supported that systemically delivered T_H1-promoting immunotherapy induced systemic effects, acting in tumor-free tissues to trigger similar inflammatory pathways to those induced in the tumor.

IL-12 and IFN-γ were interdependent and causative of inflammatory pathology

aCD40 treatment causes liver toxicity in mice, and this irAE is also observed in patients on T_H1-promoting immunotherapies (*1*, *16*, *19*–*21*). IL-12 and IFN-γ induction in the liver was consistently robust after aCD40. Hence, we dissected mechanisms of toxicity in this site.

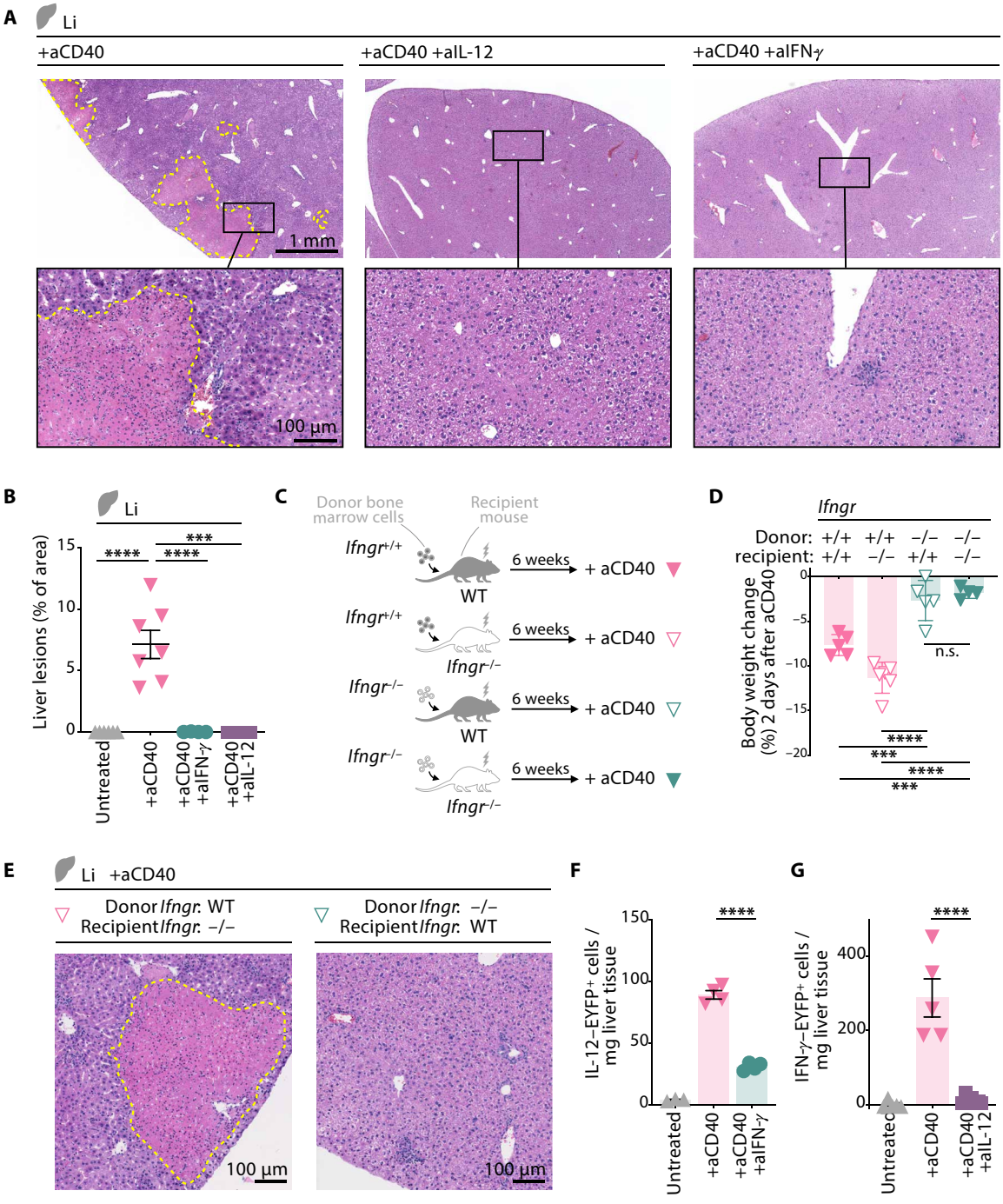

Fig. 2. IL-12 and IFN-γ cross-talk after immunotherapy was causative of inflammatory pathology. (**A**) H&E staining of fixed liver tissue from mice treated with aCD40, with or without IL-12 or IFN-γ neutralization, 2 days after aCD40. Necrotic lesions (dashed yellow lines). (**B**) Quantification of necrotic lesion area as a percentage of total liver area in H&E section ($n = 3$ to 7 mice per group). (**C**) Diagram depicting generation of bone marrow chimeras to study the requirement for IFNgR1 signaling on hematopoietic versus radio-resistant cells. (**D**) Changes in body weight from mice as depicted in (C), 2 days after aCD40 ($n = 4$ to 6 mice per group). (**E**) H&E staining of fixed liver tissue from mice sufficient for IFNgR1 only in hematopoietic cells (left) or only in radio-resistant cells (right). Necrotic lesions (dashed yellow lines). (**F**) Flow cytometry quantification of IL-12–EYFP$^+$ cells in livers of mice treated or not with aCD40, with or without IFN-γ neutralization ($n = 3$ to 4 mice per group). (**G**) Flow cytometry data as in (F) but from IFN-γ–EYFP mice with or without IL-12 neutralization ($n = 5$ to 6 mice per group). Data are represented as means ± SEM. For comparisons between two groups, Student's two-tailed *t* test was used. For comparisons between multiple groups, one-way ANOVA was used. ***$P < 0.001$; ****$P < 0.0001$.

Histological analysis showed that liver damage featured portal and prominent lobular hepatitis and broad, confluent areas of necrosis (Fig. 2A). Pathology was linked to IL-12 and IFN-γ induction, because neutralizing either cytokine eliminated liver necroinflammatory lesions (Fig. 2, A and B). In another site of irAE, the gastrointestinal tract, aCD40 led to colon crypt hyperplasia in the days after treatment, which was also abrogated by neutralizing IL-12 (fig. S3, A and B). Thus, both IL-12 and IFN-γ drove irAEs in the mouse liver and other tissues.

Because IFN-γ may act on immune cells or directly upon parenchymal cells (*22*), we used bone marrow chimeras to interrogate the importance of each (Fig. 2C). We found that nonhematopoietic (radiation-resistant) cells did not need to sense IFN-γ for liver damage or weight loss to progress; however, IFN-γ sensing by hematopoietic cells was necessary and sufficient for toxicity (Fig. 2, D and E). Although a proportion of recipient-derived F4/80^{+} CD11b$^{lo/-}$ macrophages remained as radio-resistant cells after immune reconstitution (fig. S4A), this represented a minority of macrophages, and in mice reconstituted with IFNgR1-deficient bone marrow, residual wild-type (WT) cells were not sufficient to reproduce a "wild-type" toxicity phenotype. Chimerism of myeloid cells recruited to the liver was near complete (fig. S4B). We therefore established that immune cell, rather than parenchymal cell, sensing of IFN-γ was critical for liver toxicity.

Cytokine neutralization indicated that IL-12 and IFN-γ operated in a positive-feedback manner in the liver after aCD40 treatment, similar to these cytokines' interactions in the tumor (*7*) after immunotherapy (Fig. 2, F and G). We investigated two additional tissue sites—the bone marrow, which harbored robust induction of both cytokines, and the lungs, where cytokine induction was less extreme—and observed the same interdependence between these cytokines (fig. S5, A and B). Thus, IL-12 and IFN-γ cooperatively

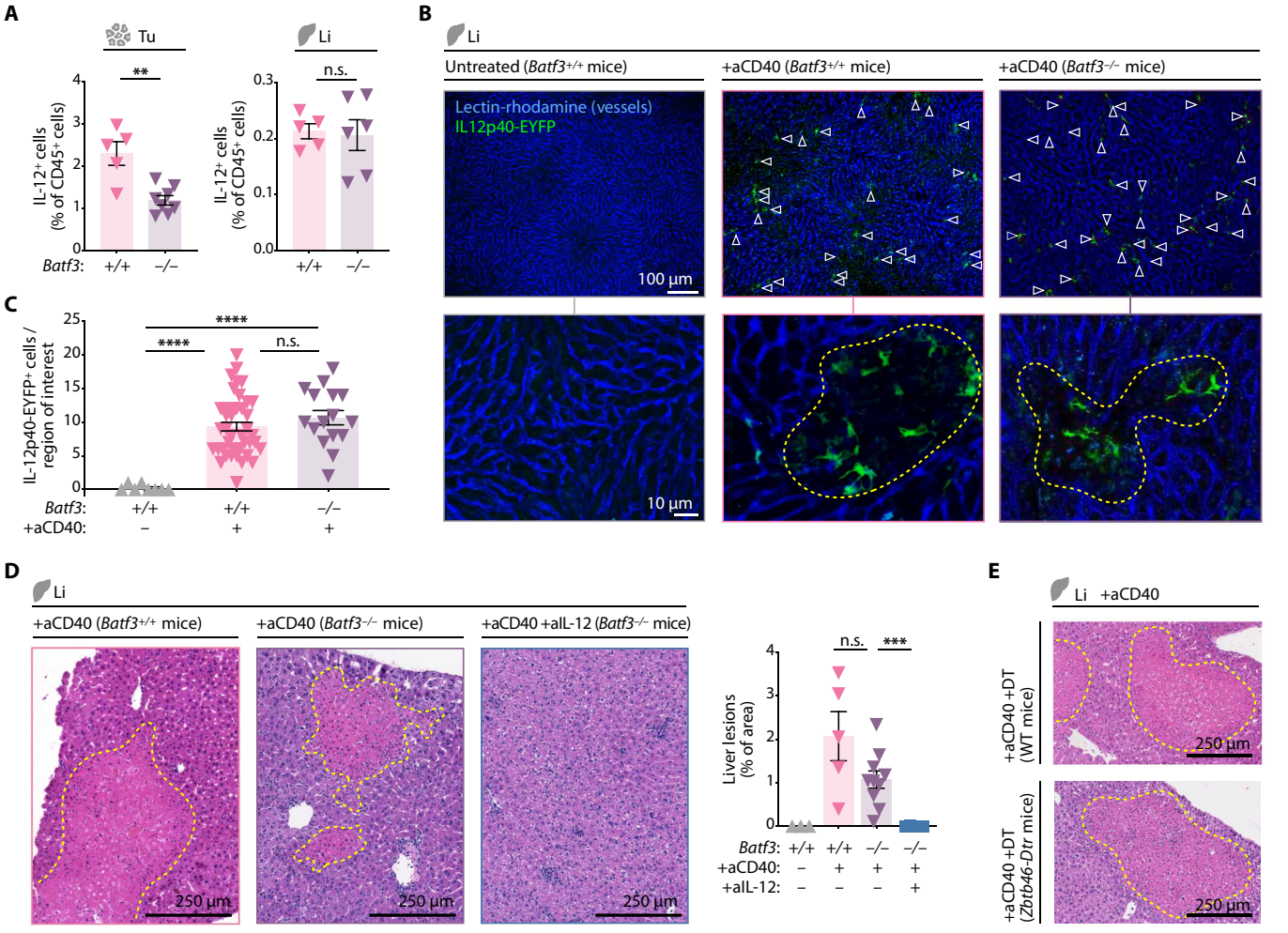

Fig. 3. DC-independent sources of IL-12 were sufficient to drive toxicity. (**A**) Intracellular IL-12p40 staining from tumors (left) or livers (right) of *Batf3*$^{+/+}$ or *Batf3*$^{-/-}$ mice 2 days after aCD40 ($n = 5$ to 8 mice per group). (**B**) Whole-mount imaging of livers from *Batf3*$^{+/+}$ *Il12p40-Eyfp* or *Batf3*$^{-/-}$ *Il12p40-Eyfp* mice, given or not aCD40, 2 days after treatment. Lectin-rhodamine (blue); IL-12–EYFP (green). Tissue lesions (dashed yellow lines). (**C**) Quantification of IL-12–EYFP^{+} cells from livers of mice as in (B). (**D**) H&E staining of livers from *Batf3*$^{+/+}$ or *Batf3*$^{-/-}$ mice treated with aCD40, with or without IL-12 neutralization, 2 days after aCD40, quantified as in Fig. 2B ($n = 3$ to 10 mice per group). Necrotic lesions (dashed yellow lines). (**E**) H&E staining of liver tissue taken from WT mice or *Zbtb46-Dtr* bone marrow chimeras treated with aCD40. Necrotic lesions (dashed yellow lines). Data are represented as means ± SEM. For comparisons between two groups, Student's two-tailed *t* test was used. For comparisons between multiple groups, one-way ANOVA was used. $^{**}P < 0.01$; $^{***}P < 0.001$; $^{****}P < 0.0001$.

drove tissue-damaging immune responses in both the tumor and in sites of toxicity, with IFN-γ sensing by immune cells representing a key event driving toxic inflammation.

Dendritic cell–independent sources of IL-12 were sufficient to drive toxicity

Tumor control in many models of immunotherapy requires *Batf3*-dependent cross-presenting type 1 conventional dendritic cells (cDC1s) and antigen-specific $CD8^+$ T cells (*23*–*25*). It is thought that *Batf3*-dependent cDC1s can give rise to IL-12–producing DC3s (*26*, *27*), also called mregDC (*8*), and $LAMP3^+$ DC (*28*); these account for most tumor-infiltrating IL-12–producing cells and are associated with antitumor immune activation (*7*, *26*, *27*). We therefore asked whether *Batf3* deficiency affected IL-12 production and toxicity in the liver after aCD40.

Batf3 deficiency abrogated tumor control after aCD40 (fig. S6A) and limited the proportion of IL-12^+ immune cells in the tumor compared with *Batf3*-sufficient mice (Fig. 3A and fig. S6C). Conversely, we observed no deficiency in IL-12–producing cells in the livers of knockout mice compared to WT controls (Fig. 3, A to C). In *Batf3*-sufficient mice, IL-12p40–$EYFP^+$ cells were detected proximally to areas of structural aberration in the inflamed liver, along with an accumulation of labeled aCD40 2 days after treatment (Fig. 3B and fig. S7, A and B). In *Batf3*$^{-/-}$ *Il12p40-Eyfp* mice, we found no major difference in prevalence or distribution of $EYFP^+$ cells (Fig. 3, B and C). Histological examination showed that *Batf3* deficiency did not prevent liver necrosis after aCD40, and IL-12 neutralization showed that necrosis was caused by *Batf3*-independent sources of IL-12 (Fig. 3D). *Batf3* deficiency likewise did not eliminate weight loss after aCD40, although it did somewhat diminish this effect (fig. S6B). We further interrogated the role of cDCs in liver toxicity using *Zbtb46-Dtr* bone marrow chimeras, enabling specific depletion of cDCs (*29*). These mice and their cDC-sufficient counterparts similarly developed liver toxicity, indicating that *Zbtb46*-dependent cells were not required for driving the irAE (Fig. 3E).

Rag2 deficiency and antibody-mediated lymphocyte targeting indicated that toxicities were CD8 and *Rag2* independent, in contrast to tumor control, which required both (fig. S8, A to D). Toxicity was independent of B, $CD4^+$ and natural killer cells (NK cells) (fig. S8, A and C). The latter two, alongside *Rag2* and $CD8^+$ cell data, suggested that lymphoid sources of IFN-γ in the liver were likely diverse and redundant after aCD40. Tumor control was preserved with B cell deficiency as well as with $CD4^+$ and NK cell targeting (fig. S8, B and D).

Resident Kupffer cells were a source of IL-12

We next interrogated the identities of IL-12–producing cells in an unbiased manner using single-cell RNA sequencing (scRNA-seq). By comparing IL-12p40–$EYFP^+$ cells in the liver and tumor after aCD40, we probed whether toxicity-associated IL-12 producers were distinct from antitumoral IL-12^+ cells in the tumor microenvironment (Fig. 4A). Visualizing IL-12^+ cells from the liver and tumor together showed that these sites contained similar and distinct IL-12^+ states (Fig. 4, A and B, and fig. S10, A to D). Both tissues included cells expressing transcripts associated with the DC lineage (*Batf3*, *Zbtb46*, and *Flt3*) and, more precisely, the DC3 state as defined by Zilionis *et al.* (*26*) (*Fscn1* and *Ccr7*) (Fig. 4, B to D; fig. S9, A to D; and tables S1 and S2). Nearly all IL-12^+ cells in tumors resembled DC3s, in line with our previous findings (*7*). However, those in the liver showed additional heterogeneity, harboring transcripts associated with macrophage identity (*Cd68*, *C1qa*, and *Apoe*) (Fig. 4, B to D, and fig. S9, A to D), as well as transcripts canonically associated with Kupffer cell (KC) identity (*Nr1h3*, *Spic*, and *Hmox1*) (Fig. 4, B to D, and fig. S9, A and B) (*30*).

In sorting IL-12p40–$EYFP^+$ cells for scRNA-seq, we used a restrictive gating strategy to optimize capture of viable cells and minimize debris (fig. S10A). However, in our flow cytometry studies, which used additional phenotypic markers and a different gating scheme, we observed an abundance of liver IL-12^+ cells with a $CD11b^{-/low}$ $F4/80^+$ phenotype (fig. S10B). These cells, thereafter referred to as IL-12^+ KCs, were likely not efficiently recovered during sorting for scRNA-seq, effectively enriching for IL-12^+ DC-like cells rather than IL-12^+ KCs. In our subsequent flow cytometry analyses, wherein we used for example a broader initial forward scatter/side scatter gate and incorporated these cells, we observed that KCs constituted the major $EYFP^+$ subset in the liver (Fig. 4, E and F, and fig. S11A). We confirmed these findings by intracellular staining with an anti–IL-12p40 monoclonal antibody (mAb) (fig. S11, B and C).

We next assessed whether the cells appearing as IL-12^+ KCs by flow cytometry were tissue resident, which would support their identity as true KCs, rather than infiltrating cells adopting a KC-like phenotype upon arrival in the liver. We tested for IL-12^+ KC residency using parabiosis. In the setting where *Il12p40-Eyfp* mice and WT mice are surgically joined, all $EYFP^+$ cells recovered from the WT parabiont must be derived from shared circulation with the $EYFP^+$ reporter mouse. Our analysis of the WT parabiont revealed a marked paucity of chimeric IL-12p40–$EYFP^+$ $CD11b^{-/low}$ $F4/80^+$ KC-like cells in the liver after aCD40, compared with $F4/80^+$ $CD11b^{hi}$ macrophages, which exhibited efficient chimerism (Fig. 4, G to I) and are thought to be derived from circulating $Ly6C^{high}$ monocytes (*31*). Consequently, most of the IL-12^+ $CD11b^{-/low}$ $F4/80^+$ cells did not derive from the circulation, supporting that they were tissue resident and therefore bona fide KCs (Fig. 4, H and I). Together, these findings supported that resident KCs were a major source of IL-12 in the liver.

IFN-γ–responsive, IL-12–producing KCs, but not DCs, dictated toxicity

We next addressed which IL-12^+ populations contributed to liver toxicity. Considering the importance of cDCs in IL-12–dependent immune responses (*32*), we designed a condition wherein *Zbtb46*-dependent cDCs were specifically unable to produce IL-12, whereas other IL-12^+ cells, including KCs, were preserved (Fig. 5, A and B). With this approach, we validated that IL-12^+ KCs were ontogenically distinct from cDCs and also identified that mice developed similar liver toxicity in the presence or absence of IL-12^+ cDCs (Fig. 5C). These data indicated that IL-12 production from cDCs was not a requirement for T_H1-driven liver toxicity.

To test the importance of IL-12 produced by macrophages, we sought to manipulate these cells while sparing DCs. First, we used clodronate liposomes (Clo. Lip.) to deplete the macrophages selectively. This treatment profoundly decreased the number of KCs (fig. S12A) and, by extension, IL-12^+ KCs (Fig. 5D), while preserving IL-12^+ DCs (Fig. 5D). Macrophage depletion eliminated liver necrosis after aCD40 (Fig. 5E). Although we considered that suppression of toxicity with Clo. Lip. could be linked to a deficiency in Fc receptors, which enable the action of aCD40 in vivo (*33*), we did not see that aCD40 was rendered inert in the setting of macrophage

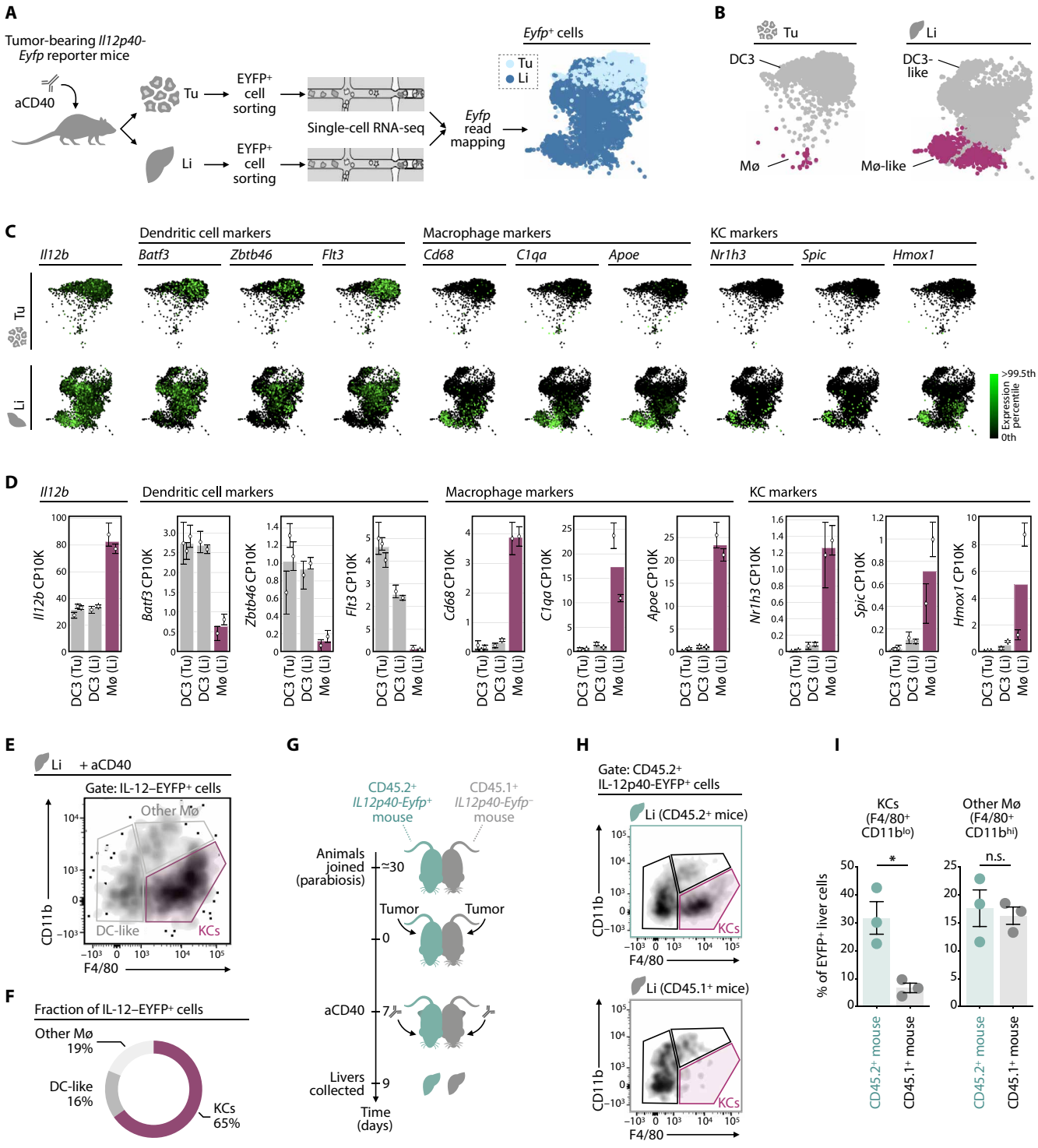

Fig. 4. Resident KCs were a source of IL-12. (**A**) scRNA-seq pipeline (left) and uniform manifold approximation and projection (UMAP) representation (right) comparing tumor and liver IL-12–EYFP$^+$ cells from aCD40-treated reporter mice (light blue, tumor, $n = 3$ mice; dark blue, liver, $n = 2$ mice). (**B**) UMAP of *Eyfp*$^+$ cells in tumor ($n = 2295$ cells) and liver ($n = 5157$ cells) colored by cell state annotation. (**C**) *Il12b* expression and DC, macrophage, and KC markers in *Eyfp*$^+$ cells from (A). Colorbar saturated at the 99.5th expression percentile measured across all *Eyfp*$^+$ cells in tumor or liver. (**D**) Quantification of transcripts depicted in (C) across *Eyfp*$^+$ cell states. Mean of each biological replicate is shown (dots) with SE of each replicate-specific mean; CP10K, count per 10,000. (**E**) Flow cytometry of liver IL-12–EYFP$^+$ cells from aCD40-treated reporter (representative example of $n = 4$ mice). (**F**) Contribution of IL-12–EYFP$^+$ cells with different myeloid cell phenotypes as defined in (E) (average from $n = 4$ mice). (**G**) Schematic for parabiosis study to analyze chimerism of liver EYFP$^+$ cells after aCD40. (**H**) Flow cytometry data gating IL-12–EYFP$^+$ CD11b$^{-/lo}$ F4/80$^+$ KCs in IL-12 reporter (top) and nonreporter (bottom) livers. (**I**) Proportions of EYFP$^+$ cells with a KC (CD11b$^{-/lo}$ F4/80$^+$) or migratory macrophage (CD11b$^+$ F4/80$^+$) phenotype in each parabiont ($n = 3$ mice per group). Data are represented as means ± SEM. For comparisons between two groups, Student's two-tailed *t* test was used. *$P < 0.05$.

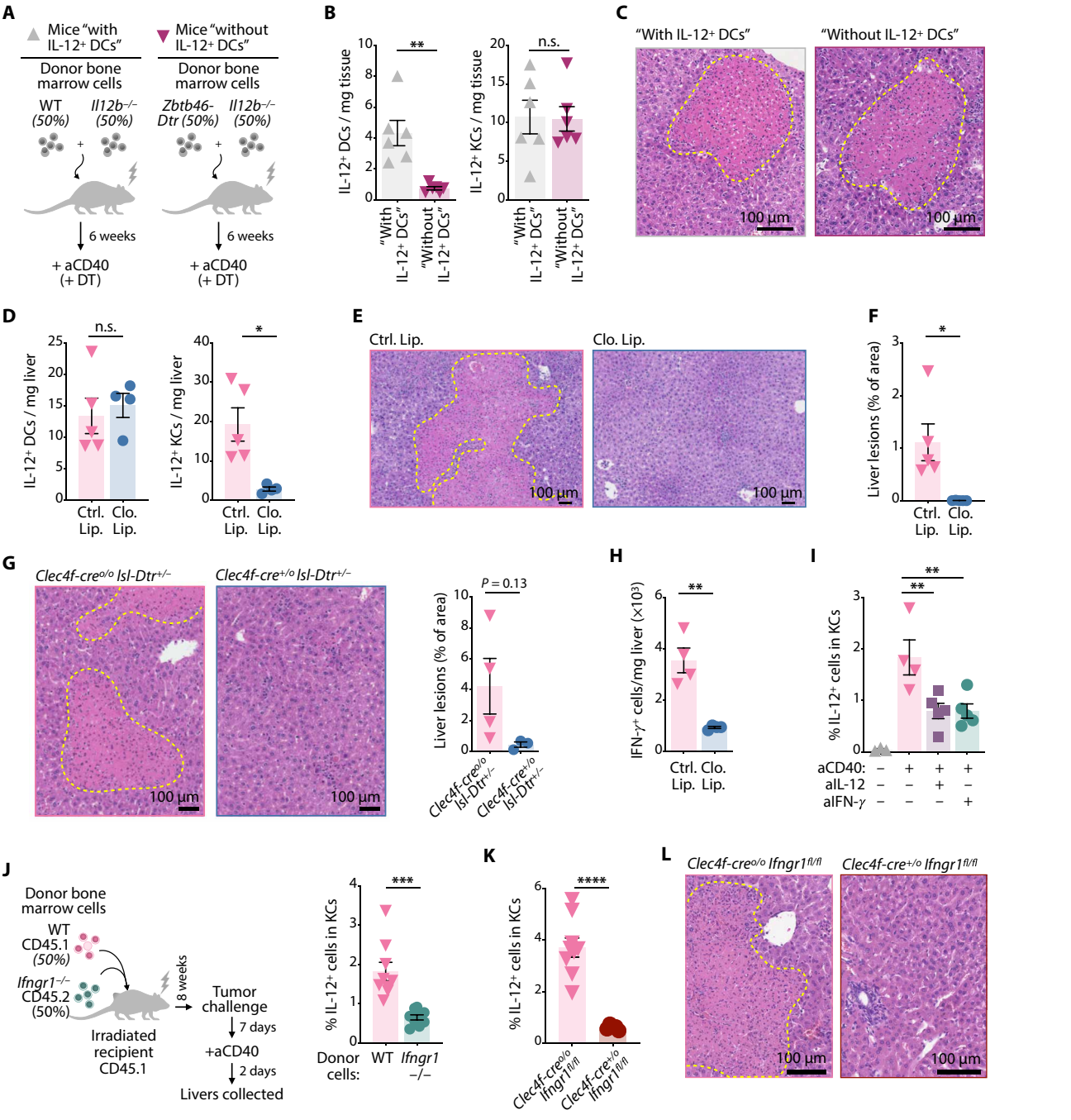

Fig. 5. IFN-γ–sensing KCs drove liver toxicity. (**A**) Schematic for bone marrow chimeras sufficient or deficient for IL-12–producing cDCs. (**B**) Quantification of IL-12–producing DCs (left) or KCs (right) from livers of mice shown in (A) 2 days after aCD40. (**C**) H&E of livers from mice as depicted in (A). Necrotic lesions (dashed yellow lines). (**D**) Flow cytometry quantification of IL-12–producing DCs (F4/80$^-$ CD11c$^+$ MHCII$^+$) or KCs (CD11b$^{-/lo}$ F4/80$^+$), 2 days after aCD40, given control or Clo. Lip. ($n = 4$ to 5 mice per group). (**E**) H&E of livers from aCD40-treated mice given control or Clo. Lip. Necrotic lesions (dashed yellow lines). (**F**) Quantification of lesions as shown in (E) ($n = 5$ mice per group). (**G**) H&E with quantification from livers of control (left) or *Clec4f-cre*$^{+/o}$ *Isl-Dtr*$^{+/-}$ (right) mice 2 days after aCD40 ($n = 3$ to 4 mice per group). Necrotic lesions (dashed yellow lines). (**H**) Flow cytometry quantification of liver IFN-γ–EYFP$^+$ cells from mice given control or Clo. Lip., 2 days after aCD40 ($n = 4$ mice per group). (**I**) Flow cytometry quantification of liver IL-12–producing CD11b$^{-/lo}$ F4/80$^+$ cells from mice treated or not with aCD40, with or without IL-12 or IFN-γ neutralization ($n = 3$ to 5 mice per group). (**J**) Diagram of mice containing both WT and *Ifngr1*$^{-/-}$ hematopoietic cells (left). Flow cytometry data comparing IL-12 production in *Ifngr1*$^{+/+}$ versus *Ifngr1*$^{-/-}$ CD11b$^{-/lo}$ F4/80$^+$ KCs from livers of bone marrow chimeras 2 days after aCD40 (right). (**K**) Flow cytometry data comparing IL-12 production in CD11b$^{-/lo}$ F4/80$^+$ KCs from livers of *Clec4f-cre*$^{o/o}$ *Ifngr1*$^{fl/fl}$ versus *Clec4f-cre*$^{+/o}$ *Ifngr1*$^{fl/fl}$ mice 2 days after aCD40. (**L**) H&E of livers from *Clec4f-cre*$^{o/o}$ *Ifngr1*$^{fl/fl}$ (left) or *Clec4f-cre*$^{+/o}$ *Ifngr1*$^{fl/fl}$ (right) mice 2 days after aCD40. Necrotic lesions (dashed yellow lines). Data are represented as means ± SEM. For comparisons between two groups, Student's two-tailed *t* test was used. For comparisons between multiple groups, one-way ANOVA was used. *$P < 0.05$; **$P < 0.01$; ***$P < 0.001$; ****$P < 0.0001$.

depletion; IL-12 was still induced in other myeloid cells (i.e., DCs), indicating that the pharmacological requirements for cellular activation and IL-12 induction were not missing.

Because Clo. Lip. treatment could deplete both resident and circulation-derived macrophages, we tested a role for bona fide KCs using *Clec4f*-driven expression of the diphtheria toxin (DT) receptor and DT administration (*30*). *Clec4f-cre*$^{+/o}$ *lsl-Dtr*$^{+/o}$ mice, when compared with *Clec4f-cre*$^{o/o}$ *lsl-Dtr*$^{+/o}$ mice, showed depletion of KCs after DT injection (fig. S12, B to D), as well as suppression of liver necrosis after aCD40 (Fig. 5G). These data supported a causal role for liver-resident macrophages in aCD40-induced tissue damage.

To interrogate the position of liver macrophages in the IL-12/IFN-γ feedback interaction, we used IFN-γ reporter mice and found that Clo. Lip. treatment markedly diminished IFN-γ induction in the liver after aCD40 treatment, supporting that macrophages stimulated IFN-γ production (Fig. 5H). Second, we asked whether IFN-γ sensing by KCs was critical for their activation. IFN-γ neutralization markedly reduced the proportion of IL-12–producing KCs (Fig. 5I); IL-12 neutralization induced similar results, presumably due to IL-12's effects on IFN-γ–producing cells (Fig. 5I). Third, we asked whether KCs lacking a functional IFN-γ receptor would fail to become activated and thus produce IL-12. Using 50:50 WT:*Ifngr1*$^{-/-}$ bone marrow chimeras to directly compare KCs sufficient or deficient for IFNgR1, we found that IFNgR1-deficient KCs had diminished expression of IL-12 (Fig. 5J) and other markers of classical activation [major histocompatibility complex II (MHCII), CD80, and CD86] (fig. S13). Last, we specifically interrogated the importance of IFN-γ sensing in KCs for toxicity using *Clec4f-cre*$^{+/o}$ *Ifngr1*$^{fl/fl}$ mice. In this setting, where KCs specifically lacked IFNgR1, IL-12 production by these cells was markedly diminished (Fig. 5K) and necrosis was nearly abrogated (Fig. 5L), supporting that liver-resident KCs were activated by elevated levels of IFN-γ and that this was a critical event in driving forward liver damage after immunotherapy. Together, these findings support that tissue-resident liver macrophages can play a major role in propagating undesired immune-mediated toxicity and that they are active local participants in the IL-12–IFN-γ positive feedback reaction.

IFN-γ, IL-12, and macrophages, but not DCs, induced a toxic neutrophil response

We next used scRNA-seq to unbiasedly assess inflammation in the aCD40-treated liver. We looked beyond IL-12–producing cells at sources of IFN-γ and at broader patterns of inflammation, which we thought might indicate avenues for limiting T_H1-driven toxicity without affecting antitumor immunity. Therefore, we sorted liver CD45$^+$ cells from untreated and aCD40-treated mice and readily identified major immune cell subsets (Fig. 6A and fig. S14A). Marked changes in immune cluster prevalence and structure accompanied treatment (fig. S14B). As suspected, multiple lymphocyte populations indicated expression of IFN-γ (fig. S15, A to D), including CD4$^+$ T cells, CD8$^+$ T cells, NK cells, and both T and NK cells with transcripts indicating cell cycling (*Mki67* and *Top2a*) (fig. S15, A to D); all five clusters contributed to increased *Ifng* expression after aCD40 (fig. S15, C to E). Heterogeneity in IFN-γ$^+$ cells was confirmed by flow cytometry (fig. S16).

Neutrophils had the greatest fold increase as a percentage of sequenced cells when comparing aCD40-treated with untreated conditions (Fig. 6B). We confirmed this increase by flow cytometry (Fig. 6, C and D). The increase in liver-associated neutrophils depended on both IL-12 and IFN-γ (Fig. 6E) and was preserved in the setting of cDC depletion (Fig. 6F) but was diminished with macrophage depletion (Fig. 6G). Histological analysis further showed spatial association of myeloperoxidase-positive (MPO$^+$) cells (a proxy for neutrophil identity) with lesioned areas in the liver (Fig. 6H), indicating that these cells could be directly involved in liver pathology.

There is ample evidence that neutrophils can exert protumoral functions in the tumor microenvironment (*34*), yet they can also cause tissue damage (*35*). Therefore, we wondered whether these cells could be promoting toxicity; if this were true, neutrophil-based interventions could conceivably reduce cells with protumoral and toxic functions. To test whether neutrophils were favoring liver toxicity, we took multiple approaches to inhibit neutrophils in vivo and assessed the impact on liver damage after aCD40. First, we used an anti-Gr1 mAb (*36*), which can also deplete Ly6C$^+$ monocytes. CD11b$^+$ CXCR2$^+$ neutrophils were substantially reduced by this method, whereas we had a less dramatic effect on CD11b$^+$ CD115$^+$ monocytes in circulation (fig. S17A). Anti-Gr1 reduced necrotic lesions in the liver (Fig. 6, I and J). Second, we used an anti-Ly6G mAb, which may not efficiently deplete neutrophils at low doses (*36*) but can limit their trafficking to inflamed tissues (*37*) and may deplete at sufficiently high doses (*38*). Anti-Ly6G, with or without a CXCR2 inhibitor, similarly reduced neutrophil-like cells in the liver (fig. S17B) and suppressed necrotic lesioning (Fig. 6, I and K). Third, we took a genetic approach, using *Csf3r*$^{-/-}$ mice, which have a deficiency in neutrophils (*39*). *Csf3r* deficiency substantially reduced liver-associated neutrophils after aCD40 but did not significantly affect liver DCs, KCs, or other macrophages (fig. S18). The absence of CSF3R reduced necrotic lesioning in the liver (Fig. 6L). These various approaches supported the notion that neutrophils exacerbated liver necrosis after aCD40.

None of the pharmacological approaches to neutrophil inhibition impeded tumor control after aCD40 (Fig. 6M). Furthermore, IL-12 and IFN-γ expression in the liver remained unchanged with anti-Ly6G (Fig. 6, N and O), showing that targeting neutrophils could limit liver damage even in the setting of robust IL-12 and IFN-γ production. This raised the possibility that toxicities associated with activation of IL-12 and IFN-γ signaling could depend on the reactivity of neutrophils to this response, rather than the cytokines themselves. Also, targeting of neutrophils revealed a potentially powerful avenue for separating antitumor effects from toxicity.

Tnf-expressing, IFN-γ–responsive neutrophils determined liver toxicity

Neither genetic nor pharmacological approaches achieved complete inhibition of neutrophils. This could explain the incomplete rescue of liver inflammation with these interventions (Fig. 6I). We therefore thought to target effector functions of neutrophils rather than the cells themselves in an attempt to stem their pathogenicity.

When we compared differentially expressed genes between aCD40-treated versus untreated neutrophils (fig. S19A and table S3) and assessed enriched gene ontology (GO) terms, we found positive regulation of tumor necrosis factor (TNF) production to be significantly enriched in neutrophils from the treated condition (Fig. 7A). *Tnf* was among the top enriched transcripts in aCD40-treated compared with untreated neutrophils (Fig. 7B and fig. S19A). In addition, neutrophils were the cell type producing this transcript at the highest level on a per-cell basis (fig. S19B). When factoring in the abundance of diverse immune populations in the inflamed liver, we

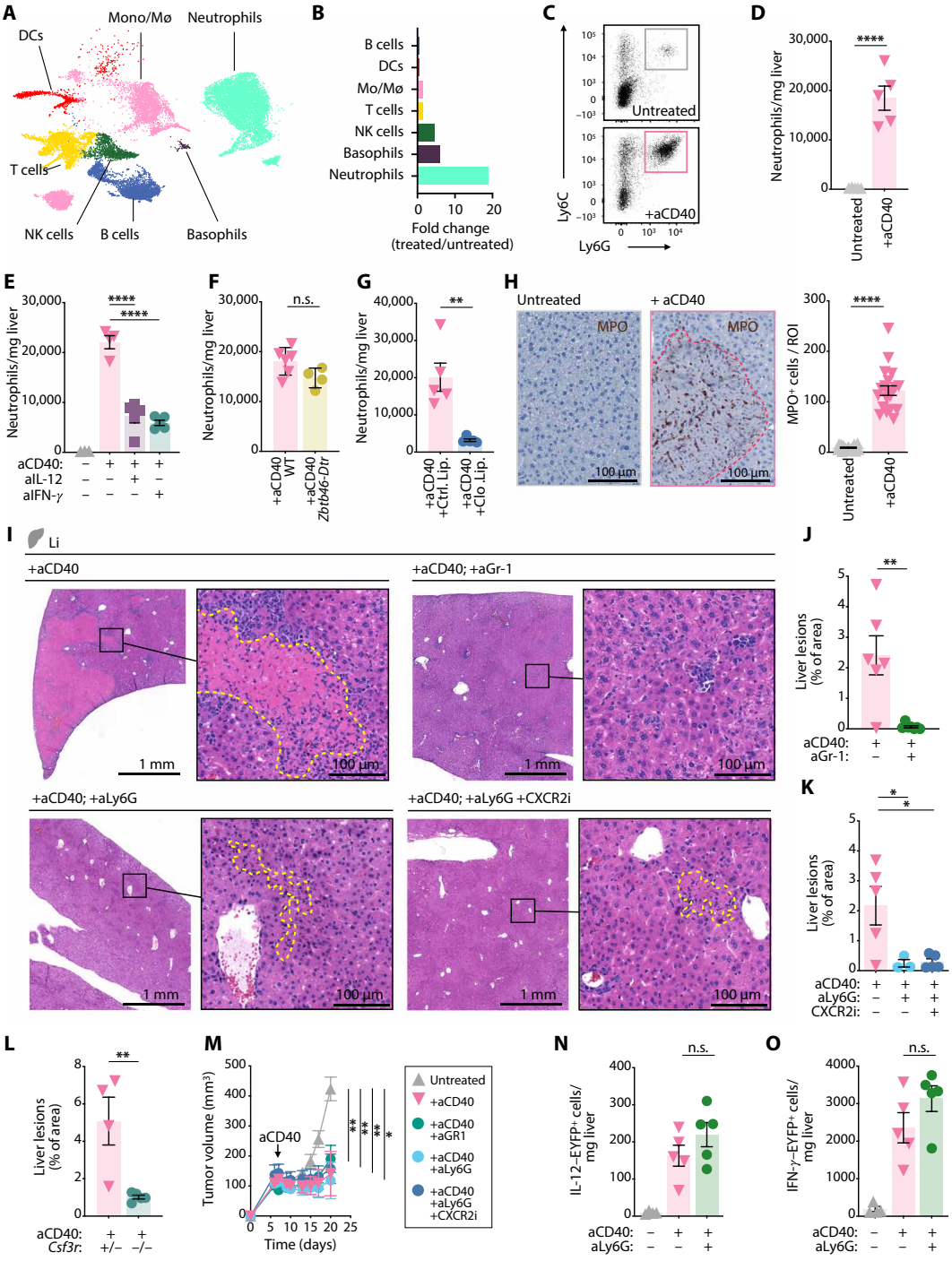

Fig. 6. IFN-γ, IL-12, and macrophages, but not DCs, induced a pathogenic neutrophil response. (**A**) UMAP of CD45$^+$ cells from livers of untreated (n = 5879 cells) or aCD40-treated (n = 12,892 cells) mice, colored by major cell type (n = 2 mice per condition). (**B**) Fold change in the relative abundance of major cell types in sequenced CD45$^+$ cells from livers of aCD40-treated versus untreated mice. (**C**) Flow cytometry data of neutrophils (Ly6C$^+$ Ly6G$^+$) in livers of untreated or aCD40-treated mice. (**D**) Quantification of flow cytometry data as shown in (C) (n = 5 mice per group). (**E**) Flow cytometry quantification of liver neutrophils from mice treated or not with aCD40, with or without IL-12 or IFN-γ neutralization (n = 3 to 5 mice per group). (**F**) Flow cytometry quantification of liver neutrophils from WT or *Zbtb46-Dtr* mice after aCD40 (n = 4 to 6 mice per group). (**G**) Flow cytometry quantification of liver neutrophils from mice treated with aCD40 and control or Clo. Lip. (n = 5 mice per group). (**H**) MPO staining of livers from untreated and aCD40-treated mice. ROI, region of interest (n = 5 mice per group). Necrotic lesions (dashed red lines). (**I**) H&E staining of livers from aCD40-treated mice, given (or not) anti–Gr-1 or anti-Ly6G mAbs with or without a CXCR2 inhibitor (CXCR2i). Necrotic lesions (dashed yellow lines). (**J**) Quantification of liver lesions from aCD40-treated mice, given (or not) anti–Gr-1 mAbs (n = 6 to 7 mice per group). (**K**) Quantification of liver lesions from aCD40-treated mice, given (or not) anti-Ly6G mAbs with or without a CXCR2 inhibitor (n = 3 to 5 mice per group). (**L**) Quantification of liver lesions from aCD40-treated mice sufficient or deficient for *Csf3r* (n = 4 to 5 mice per group). (**M**) MC38 tumor volumes for mice treated (or not) with aCD40, with or without neutrophil targeting. (n = 6 to 8 mice per group) (**N**) Flow cytometry quantification of IL-12–EYFP$^+$ cells in livers of mice treated (or not) with aCD40, given or not anti-Ly6G mAbs (n = 4 to 5 mice per group). (**O**) Flow cytometry quantification of IFN-γ–EYFP$^+$ cells in livers of mice treated (or not) with aCD40, given or not anti-Ly6G mAbs (n = 4 to 5 mice per group). Data are represented as means ± SEM. For comparisons between two groups, Student's two-tailed t test was used. For comparisons between multiple groups, one-way ANOVA was used. *P < 0.05; **P < 0.01; ****P < 0.0001.

found that neutrophils contributed ~92% of all *Tnf* detected (Fig. 7C). Consequently, neutrophils appeared to be the primary source of *Tnf* in the liver after aCD40.

We therefore hypothesized that neutralizing TNF-α might eliminate a key pathogenic effector function of neutrophils. Anti–TNF-α prevented body weight loss triggered by aCD40 (fig. S20A), in accordance with previous observations (*14*), and abrogated liver necrosis (Fig. 7D). Liver neutrophils in aCD40-treated mice showed high expression of both *Tnfrsf1a* and *Tnfrsf1b* (fig. S21), suggesting a possible feed-forward loop of TNF-α onto neutrophils themselves. In favor of this hypothesis, we found a marked reduction in neutrophils in the context of anti–TNF-α treatment (fig. S20B). Limiting

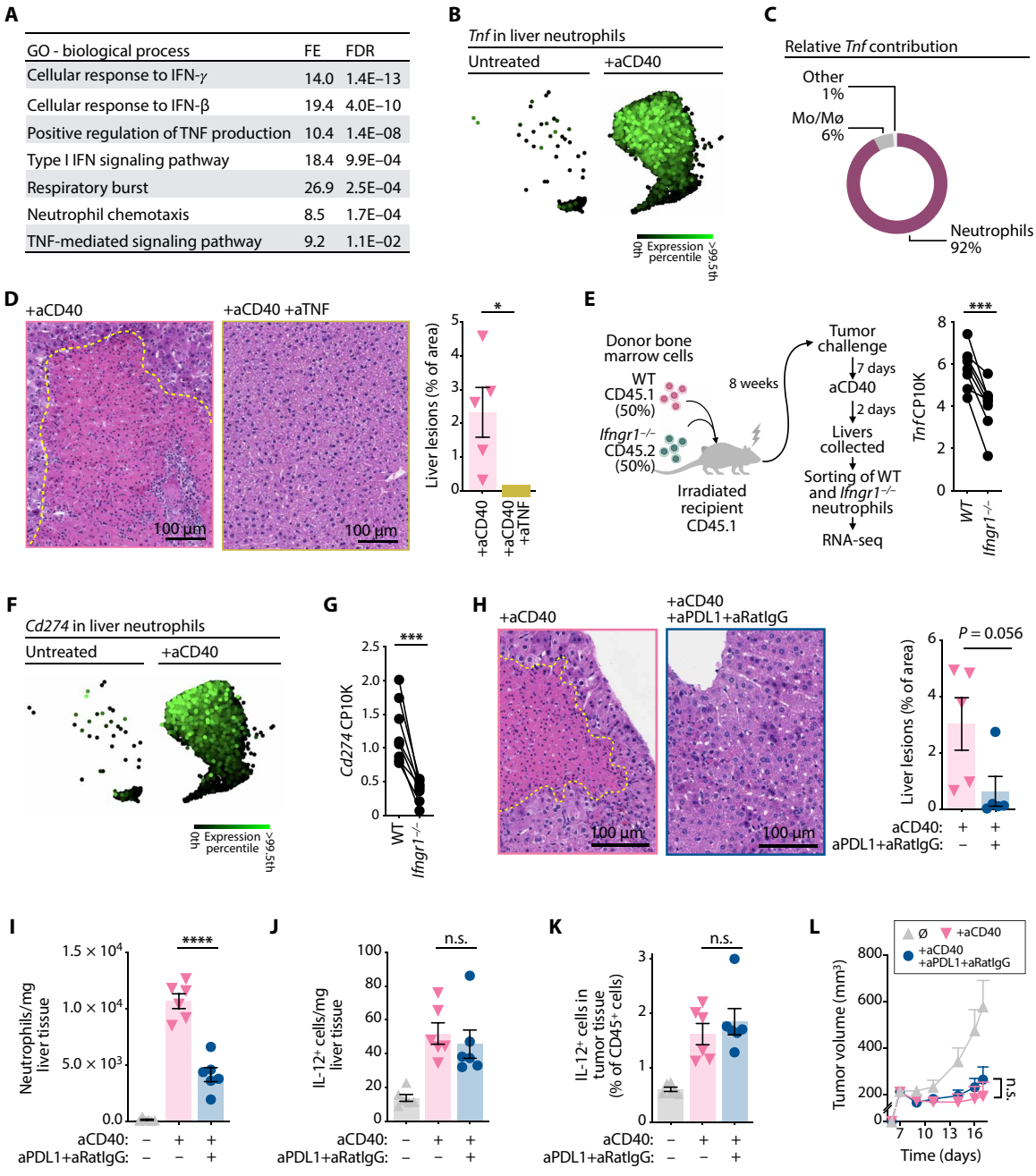

Fig. 7. TNF-α–expressing, IFN-γ–responsive neutrophils determined toxicity but not tumor control. (**A**) GO results based on scRNA-seq transcripts significantly enriched in liver neutrophils from aCD40-treated compared with untreated mice. FE, fold enrichment; FDR, false discovery rate. (**B**) Single-cell expression of *Tnf* in liver neutrophils from mice treated or not with aCD40. Colorbar saturated at 99.5th expression percentile measured across all CD45$^+$ immune cells. (**C**) Relative contributions by different cell types to *Tnf* transcription based on transcript counts and relative representation of each cell type. (**D**) H&E staining, with quantification, of livers from aCD40-treated mice, with or without TNF-α neutralization ($n = 5$ mice per group). Necrotic lesions (dashed yellow lines). (**E**) Diagram of mice containing both WT and *Ifngr1*$^{-/-}$ neutrophils. Both populations were sorted from livers 2 days after aCD40 and processed for RNA-seq (left). Quantification of *Tnf* transcripts (gene of interest) in these cells (right). (**F**) Single-cell expression of *Cd274* in liver neutrophils from mice treated (or not) with aCD40. Colorbar as in (B). (**G**) Quantification of *Cd274* transcripts (gene of interest) from WT and *Ifngr1*$^{-/-}$ neutrophils from livers of mice in (E). (**H**) H&E staining, with quantification, of livers from aCD40-treated mice, given (or not) anti–PD-L1 followed by anti-rat IgG2b-depleting mAbs ($n = 5$ mice per group). Necrotic lesions (dashed yellow lines). (**I**) Flow cytometry quantification of liver neutrophils from mice treated (or not) with aCD40, given (or not) anti–PD-L1 followed by anti-rat IgG2b-depleting mAbs ($n = 6$ mice per group). (**J**) Flow cytometry quantification of liver IL-12$^+$ cells from mice treated as in (I) ($n = 6$ mice per group). (**K**) Flow cytometry quantification of tumor IL-12$^+$ cells from mice treated as in (I) ($n = 6$ mice per group). (**L**) MC38 tumor volumes for mice treated as in (I) ($n = 7$ mice per group). Data are represented as means ± SEM. For comparisons between two groups, Student's two-tailed *t* test was used. For comparisons between multiple groups, one-way ANOVA was used. *$P < 0.05$; ***$P < 0.001$; ****$P < 0.0001$.

TNF-α availability also led to a decrease in IFN-γ$^+$ and IL-12$^+$ cells (fig. S20B). The identification of neutrophils, rather than macrophages or lymphocytes, as the main *Tnf* expressers shed light on the cellular source of this toxic mediator and highlighted a mechanism of neutrophil pathogenicity in the context of irAEs. Furthermore, the marked effects of TNF neutralization in our model illustrated the pleiotropic effects that this cytokine can have on driving forward toxic inflammation.

We further asked whether pathogenic neutrophils responded to key elements of T_H1 inflammation. In our GO analysis of aCD40-treated versus untreated liver neutrophils, we identified multiple pathways indicating responsiveness to IFNs, notably IFN-γ (Fig. 7A). Using 50:50 bone marrow chimeras to directly compare neutrophils sufficient or deficient for the IFN-γ receptor that coexisted in the same hosts (Fig. 7E), we observed similar numbers of WT and *Ifngr1*$^{-/-}$ neutrophils in livers on day 2 after aCD40 (fig. S22A), indicating that IFNgR1 did not control the neutrophil response quantitatively; however, *Ifngr1*$^{-/-}$ neutrophils showed significantly less *Tnf* expression compared with their WT counterparts (Fig. 7E). These data indicated that IFN-γ sensing by neutrophils contributed to their *Tnf* production.

In addition to *Tnf*, we found that transcripts associated with oxidative burst (*Cybb*, *Nos2*, *Acod1*, and *Sod2*), proinflammatory cytokines and chemokines (*Cxcl9*, *Cxcl10*, and *Il27*), and IFN-responsive factors (*Ifi47* and *Tap1*) were also expressed at lower levels in *Ifngr1*$^{-/-}$ neutrophils compared with WT neutrophils (fig. S22B), overall indicating that IFN-γ sensing favored a particular inflammatory transcriptional program in liver neutrophils.

Neutrophils in aCD40-treated livers also showed high expression of the canonical IFN-γ–responsive transcript *Cd274* [encoding programmed death-ligand 1 (PD-L1); Fig. 7F], which depended on IFN-γ sensing (Fig. 7G). Furthermore, both scRNA-seq (Fig. 7F) and flow cytometry (fig. S23, A and B) readouts indicated that only a subset of neutrophils strongly up-regulated *Cd274*/PD-L1 after aCD40 treatment, suggesting that PD-L1 may mark IFN-γ–responsive, proinflammatory neutrophils. We thus sought to experimentally remove these cells by using an anti–PD-L1–mediated cell depletion approach. To this end, aCD40-treated mice received anti–PD-L1, followed by a depleting isotype of anti-rat immunoglobulin G2b (IgG2b). In this setting, liver necrosis was reduced (Fig. 7H), consistent with a reduction in liver-associated neutrophils (Fig. 7I). The treatment also reduced some CD11b$^+$ macrophages (fig. S23C), which should be considered when interpreting our results; however, IL-12–producing populations remained unchanged in the liver (Fig. 7I and fig. S23D), supporting that we did not substantially affect upstream myeloid cell players mediating T_H1 toxicity. Furthermore, tumor-associated IL-12–producing cells were retained (Fig. 7K), and the antitumor response was not significantly affected (Fig. 7L). Together, these data situate IFN-γ–sensing neutrophils as important players in T_H1-dependent liver inflammation after aCD40 immunotherapy.

Immune checkpoint blockade–induced T_H1 responses in mice and humans

We next aimed to determine whether other T_H1-promoting immunotherapies could activate the same inflammatory pathways in tumor-free tissue. First, we assessed the livers of IL-12p40–EYFP reporter mice treated with immune checkpoint blockade (ICB) (anti–PD-1 + anti–CTLA-4). We indeed found a trend toward elevated IL-12 expression in this tumor-free site (fig. S24A), although it was of a lower magnitude than observed with aCD40, as expected, because ICB is typically well tolerated in mice. We also identified increased KC activation after ICB, indicated by higher MHCII expression (fig. S24B). Furthermore, the same ICB treatment led to an increase in liver-associated neutrophils (fig. S24C).

We next sought to investigate the clinical relevance of our findings. Because tissue samples from aCD40-treated patients are rare, we focused instead on patients who received ICB treatment and developed irAEs. We specifically investigated the hypothesis that, in humans, T_H1 activation caused by immunotherapy agents like ICBs might achieve a sufficient magnitude in tumor-free sites to cause toxicities similar to those in aCD40-treated mice. To this end, we initially made use of published scRNA-seq data from patients with melanoma experiencing ICB-induced colitis (*15*) and compared this dataset with our scRNA-seq data from mouse irAEs (table S4). We found that expression of IFN-γ– and IL-12–related transcripts correlated in both direction and degree of change between mouse and human irAEs (Fig. 8A). These parallels suggested that aspects of the lymphoid and myeloid T_H1 responses observed in the context of mouse irAE (triggered by aCD40) could occur in the clinical setting (triggered by ICBs). We additionally found that gene expression changes in liver T cells, monocytes/macrophages, and DCs from aCD40-treated mice correlated with changes seen in the corresponding cell populations from irAE colons (Fig. 8B, and fig. S25, A and B), indicating that our model of T_H1 irAEs recapitulated features of clinical irAEs. Considering these parallels, we propose that IL-12 and IFN-γ signaling may generally feature in, and even be determinants of, toxicities caused by T_H1-promoting agents, independent of therapeutic modality.

We further tested whether ICB-induced adverse events were associated with a neutrophil response in patients with cancer. For this, we could not use available ICB-induced colitis scRNA-seq data because neutrophils were removed before sequencing (*15*). However, we collected liver tissue from 24 patients with cancer who developed hepatitis in the context of ICB treatment (Fig. 8D and table S5). Histopathological analysis revealed neutrophils associated with areas of liver inflammation, as shown by hematoxylin and eosin (H&E) staining (Fig. 8D and fig. S26). Granulocytes were also visualized by MPO staining, which showed MPO$^+$ cells in inflamed areas of the livers (Fig. 8E). We confirmed granulocyte presence in irAE livers using an additional marker, CD15 (Fig. 8F and fig. S26). When we compared the histological score, graded as mild, moderate, or severe (Fig. 8D), with the neutrophil and MPO/CD15 scores, graded from 0 to 2, for each case of hepatitis, we found consistent granulocytic infiltration in both moderate and severe cases of irAE hepatitis (Fig. 8G). This suggested that granulocytic inflammation was associated with severity of inflammation. Overall, these human data indicate that, in the setting of ICB, both T_H1 cytokine activation and neutrophil accumulation remarkably correspond with diagnosis of irAEs, implicating broad clinical importance of the mechanisms of T_H1 toxicity that we revealed in aCD40-treated mice.

DISCUSSION

This study dissected the cellular and molecular mechanisms of irAEs, which are a major clinical problem. In mice treated with the T_H1-promoting immunotherapeutic drug aCD40, canonical antitumoral cytokines IL-12 and IFN-γ were induced in tumor-free tissue sites, driving a pathological inflammatory response that depended on macrophages and neutrophils. Conversely, DCs and

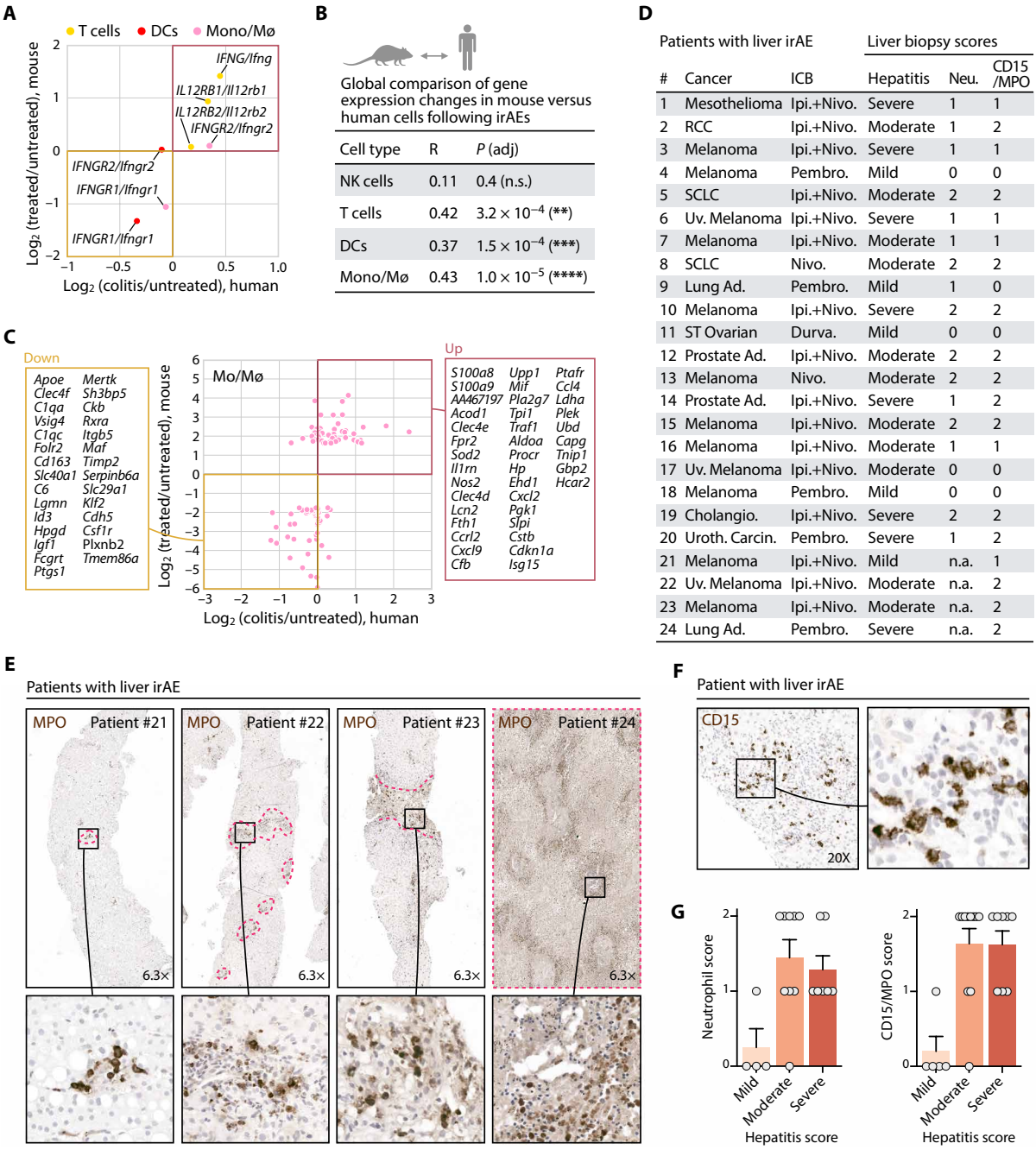

Fig. 8. IFN-γ, IL-12, and neutrophil responses in human irAEs. (**A**) Comparison of fold changes in single-cell gene expression for key cytokines and receptors in immune cells from human colon (immunotherapy-induced colitis versus patients not receiving immunotherapy) and mouse liver (aCD40-treated versus untreated). Red and yellow quadrants show conserved responses to therapy. See also table S4. (**B**) Comparison of gene expression changes in selected immune cell types from mouse livers and human colons from immunotherapy conditions as in (A). Pearson correlation (*R*) for genes changing in mice and human homologs, calculated on the basis of direction of change. The 100 genes with greatest fold change in mice were used for the analysis. See also table S4. (**C**) Scatterplot comparing changes in gene expression for monocytes/macrophages in mouse livers and human colons from immunotherapy conditions as in (A). Up to 100 genes were selected on the basis of (i) FDR < 0.05 and magnitude of change >2-fold in mouse and (ii) existence of a 1:1 human homolog. Red and yellow quadrants show conserved responses to therapy; genes with conserved responses listed. See also table S4. (**D**) Cancer diagnosis, treatment, toxicity score, and granulocyte inflammation scores from livers of 24 patients with cancer who developed liver irAEs. Additional information is available in table S5. n.a., not assessed. (**E**) MPO staining of liver tissue from four patients diagnosed with cancer, treated with ICBs, and who developed hepatitis. Dashed red lines indicate lobular hepatitis. Additional information available in table S5. (**F**) Example of CD15 staining in liver tissue from patient as in (E). Additional information is available in table S5. (**G**) Quantification of neutrophil score (left) and $CD15^+/MPO^+$ granulocyte score (right) in irAE livers from patients with cancer, treated with ICB who developed mild, moderate, or severe liver toxicities as assessed by histological analysis of liver biopsies.

$CD8^+$ T cells drove tumor control but were not required for toxicity. Our findings in mice mirrored phenotypes from human irAEs caused by ICB, showing similar immune reactions across species; the findings reported here can thus serve as an important baseline when considering mechanisms of clinical relevance.

We suggest that IFN-γ–dependent corruption of tissue-associated macrophages may broadly be a feature of irAEs triggered by T_H1-promoting immunotherapies; if a therapy boosts IFN-γ, IFN-γ–vulnerable macrophages may be activated by the local cytokine milieu, lose their tolerogenic phenotype, and propagate undesired immune activation. Our findings build upon important discoveries implicating macrophages in aCD40 liver toxicity (*40*, *41*), and models of hepatitis B infection have likewise implicated damaging consequences of KC activation and IL-12 production (*42*, *43*), highlighting the importance of these cells for balancing liver homeostasis versus pathology.

We showed that the toxic effects of IL-12 and IFN-γ could be tied to activation and effector functions of neutrophils, which were reactive to T_H1 inflammatory signals in a manner that substantially influenced their phenotype, ultimately affecting pathology progression. Neutrophil-related parameters have been proposed as biomarkers for irAEs by multiple previous studies (*44*, *45*). Here, we found these cells in both our mouse model and clinical samples, further indicating their reproducible association with this clinical problem and supporting translational relevance of the neutrophil-driven mechanisms of toxicity that we report.

Because our manipulations of neutrophils suppressed tissue damage without affecting T_H1 cytokines or tumor control, we propose that neutrophil targeting may limit irAEs without hampering antitumor immunity, especially because neutrophils are often considered to be protumoral (*34*). Multiple strategies for neutrophil targeting are being investigated in diverse clinical settings (*46*), and therapeutics such as CXCR2 inhibitors are being used in some patients with cancer (*47*). Alternatively, chemotherapy preceding immunotherapy may benefit patients in some settings, considering that this cytotoxic treatment induces neutropenia, which could limit irAEs. This idea is supported by findings from preclinical combination therapy studies, published by Byrne *et al.* (*40*). However, because chemotherapy itself may cause hepatotoxicity (*48*) and could disrupt KCs, additional studies will be needed to define whether our findings apply in the combination setting. Last, targeting TNF could also limit neutrophil-dependent toxicities, considering that these cells were the main *Tnf* expressers in our system. Our findings highlight a biological rationale for TNF targeting in the clinic and favor prioritizing anti-TNF for the management of irAEs including hepatitis.

Ultimately, there is a need to improve efficacy of cancer immunotherapy beyond current response rates, but avoiding toxicity is crucial. It is critical to understand which elements of therapy-induced immune reactions cause irAEs, so that they can be targeted without hampering antitumor T_H1 responses. With the goal to untangle the pathologic processes that so often limit clinical utility of immunostimulatory agents, here, we revealed potential pathways that may help to dissociate desired antitumor and undesired toxicity effects of immunotherapy.

MATERIALS AND METHODS

(For full methods, see the Supplementary Materials.)

Study design

This study was designed to interrogate mechanisms of T_H1 cytokine–driven pathologies that occur in nonmalignant tissues after anticancer immunotherapies. Mice were treated with the agonist aCD40, and cellular and molecular mechanisms of toxicity were delineated primarily using the time point when greatest toxicity was observed in the mice (indicated by body weight loss and gross pathology of vital organs including the liver, 2 to 3 days after immunotherapy treatment). Liver toxicity was quantified, on the basis of H&E-stained tissue sections, by calculating the percentage of tissue appearing as confluent areas of necrosis. All toxicity studies were completed in tumor-bearing mice, and mice were randomized between treatment groups based on tumor volume on day 6 or 7 of tumor growth, before treatments began. End point analyses included flow cytometry, scRNA-seq, RNA-seq, imaging, and histological analysis. Raw data from all mouse experiments are available in table S8.

Mice and tumor models

Animals were bred and housed under specific pathogen–free conditions at the Massachusetts General Hospital (MGH). Experiments were approved by the MGH Institutional Animal Care and Use Committee (IACUC) and were performed in accordance with MGH IACUC regulations. MC38 or TC-1 cells were implanted at 2×10^6 cells in the flank. After 1 week, mice were treated with aCD40 clone FGK4.5 (~5 mg/kg) (BioXCell, catalog no. BE0016-2) intraperitoneally and analyzed 2 days after treatment, unless otherwise noted. For ICB, anti–PD-1 (clone 29F.1A12) was provided by G.J. Freeman. Mice received anti–PD-1 (~10 mg/kg) and anti–CTLA-4 (~5 mg/kg) (clone 9D9, BioXCell, catalog no. BE0164) intraperitoneally on days 6 to 8 of tumor growth, and tissues were analyzed on day 9.

Flow cytometry studies

Briefly, all solid tissues were excised, minced, and digested with enzymes at 37°C before being processed through a cell strainer and resuspended for staining in phosphate-buffered saline (PBS) with 0.5% bovine serum albumin.

Cytokine and lymphocyte targeting

Cytokine-neutralizing antibodies were given at 500 μg daily starting on day 7 of tumor growth and continued for 1 to 2 days. For the TC-1 tumor study, IL-12p40 was neutralized for six consecutive days. Anti–IFN-γ was administered at 1 mg of antibody on day 7 and then 500 μg for subsequent doses.

Anti-CD4 was dosed at 100 μg per injection (BioXCell, catalog no. BE0003), anti-CD8α at 200 μg per injection (BioXCell, catalog no. BE0004), and anti-NK1.1 at 200 μg per injection (BioXCell, catalog no. BE0036) and injected every other day from days 6 to 10 of tumor growth. All injections were intraperitoneal.

Neutrophil targeting

For neutrophil targeting, antibodies/inhibitors were used as follows: anti-Gr1 (BioXCell, catalog no. BE0075) at 100 μg per dose on days 6 and 8 of tumor growth before sacrifice on day 10. Anti-Ly6G (BioXCell, catalog no. BP0075) was administered at 500 μg per mouse on day 7 (2 hours before aCD40) and then 250 μg per mouse on day 8 before sacrifice on day 9. For tumor growth studies, all mAbs were dosed one additional time on day 10. CXCR2 inhibitor

SB 225002 (Tocris, catalog no. 2725/10) was injected at 200 μg per dose and scheduled as anti-Ly6G. For IL-12 and IFN-γ reporter mice, anti-Ly6G (Absolute Antibody, catalog no. Ab00295-2.0) was dosed at 200 μg per mouse on days 6 to 8. For anti–PD-L1–based targeting of neutrophils, anti–PD-L1 (BioXCell, catalog no. BE0101) was injected at 12.5 mg/kg ~10 hours after aCD40 treatment and again 1 day after treatment, each time followed by anti-rat IgG2b (12.5 mg/kg) (BioXCell, catalog no. BE0252) ~1 hour later. All injections were intraperitoneal.

Histology

Mouse livers were fixed in 10% formalin overnight, washed twice with PBS, and placed in 70% ethanol or PBS until processing. For colons, 3 days after aCD40, tissue was isolated, flushed with cold 5% fetal bovine serum in PBS, opened longitudinally, rolled, and tied loosely with a nylon suture (Ethicon). For H&E, tissues were paraffin-embedded, sectioned, and stained with H&E at the MGH Histopathology Research Core.

Whole-mount liver imaging

On day 7 of tumor growth, mice were injected intraperitoneally with unlabeled or fluorescently labeled aCD40 mAb (mAb, BioXCell, catalog no. BE0016-2; antibody labeling kit, Thermo Fisher Scientific, catalog no. S30044). Two days later, mice were injected retro-orbitally with fluorescent lectin to label vasculature and then euthanized. IL-12p40–IRES–EYFP or IL-12p40–IRES–EYFP *Batf3*$^{-/-}$ mouse livers were excised, placed in PBS between an inverted petri dish and a microscope coverslip, and imaged using an Olympus FluoView FV1000MPE confocal imaging system (Olympus America). Images were processed using Fiji from ImageJ.

Single-cell RNA sequencing

MC38 flank tumors in IL-12p40–IRES–EYFP mice grew for 7 days, and then mice were treated or not with aCD40. Two days later, tumors and livers were processed to generate single-cell suspensions. Cells were stained for CD45 (table S7), labeled with 7-aminoactinomycin D (Sigma-Aldrich), and CD45$^+$ cells or IL-12–EYFP$^+$ cells were sorted using a BD FACSAria sorter. InDrops scRNA-seq was performed as described before (*49*) with changes to DNA primers and read lengths listed in table S6.

Parabiosis

CD45.1^{STEM} (*50*) and B6.129-*Il12*^{btm1Lky}/J (IL-12–EYFP) mice were surgically joined as previously described (*7*). Circulatory equilibrium was confirmed 3 to 5 weeks after surgery; both mice were then injected with MC38 tumors on the outer flank and 7 days later treated with aCD40; tissues were harvested 2 days later to analyze IL-12$^+$ populations.

Bone marrow transfer experiments

CD45.1 [The Jackson Laboratory catalog no. 002014 or CD45.1^{STEM} (*50*)] recipient mice were irradiated with a single dose of 1000 centigray using a cesium-137 irradiator. The next day, bone marrow from donor mice was processed for injection: For IFNgR1 deficiency experiments, either WT CD45.1 mice or CD45.2 *Ifngr1*$^{-/-}$ mice served as donors. For ZBTB46-DTR experiments, either WT (CD45.2), *Il12p40*$^{-/-}$, or *Zbtb46-Dtr* mice served as donors. Donor mouse cells were counted manually. For 50:50 chimeras, cells were mixed at a 1:1 ratio before injection. Cells were injected retro-orbitally at 10×10^6 to 14×10^6 total cells per mouse in 200- to 400-μl volume, and mice were allowed to reconstitute for 5.5 to 7.5 weeks. Chimerism was confirmed by cheek bleed before tumor challenge and immunotherapy treatment.

DT injection

Mice receiving DT (Sigma-Aldrich) were dosed at 10 ng/g of body weight initially 0.5 to 1 day before aCD40 injection and then at 4 ng/g of body weight 1 day after immunotherapy.

Clodronate liposomes

Mice receiving clodronate or control liposomes were dosed with 200 μl of liposomes (Liposoma, catalog no. P-010-010) retro-orbitally 1 day before immunotherapy and again 1 day after treatment.

Bulk RNA-seq

For RNA-seq, 50:50 WT:*Ifngr1*$^{-/-}$ bone marrow chimeras were injected with tumors and aCD40 as usual. On day 2 after treatment, livers were processed for fluorescence-activated cell sorting (FACS) and CD45.1 (WT) or CD45.2 (*Ifngr1*$^{-/-}$) neutrophils were sorted directly into TRIzol reagent and placed on ice. RNA was extracted using the TRIzol Plus RNA Purification Kit (Thermo Fisher Scientific, catalog no. 12183555). Libraries were prepared in collaboration with the Harvard Biopolymer Core Facility. Libraries were normalized in equimolar ratios for one final pool and sequenced using an Illumina NextSeq 500 instrument; samples were demultiplexed, and the resulting fastq files were analyzed using an RNA-seq pipeline implemented in the bcbio-nextgen project (https://bcbio-nextgen.readthedocs.org/en/latest/).

Gene ontology

Differentially expressed genes from aCD40-treated versus untreated liver neutrophils were entered into the GO enrichment analysis tool for *Mus musculus*, and enriched biological processes were determined with PANTHER Overrepresentation Test (released 28 July 2020) using Fisher's exact test; annotation version and release date: GO Ontology database DOI: 10.5281/zenodo.4081749 (released 9 October 2020) (*51*–*53*).

Human liver samples

Patient selection and inclusion criteria

Patients on immune checkpoint therapy who developed hepatic irAEs were identified through the Oncology Department of the Lausanne University Hospital and the Hospital of the University of Geneva. All included patients had given their written informed consent for reuse of their medical and histopathological data, with the exception of deceased persons.

Patient characterization

Demographic, clinical, laboratory, and histopathological data were retrieved from electronic medical records and archives.

Histopathology and immunochemistry

Liver biopsy or autopsy samples were fixed in 10% formalin and paraffin-embedded, and 3- to 5-μm-thick sections were stained as follows: for cases 1 to 20, H&E and CD15 (clone: BD Pharmingen MMA, dilution 1:1500); for patients 21 to 24, MPO (clone: DAKO A0398, dilution 1:1000) and CD15 (Ventana). Cases were scored for severity, neutrophilic infiltration, and CD15/MPO positivity.

Statistical analysis of flow cytometry, histology, or tumor burden data

All statistical analyses were performed using GraphPad Prism software. Results were expressed as means ± SEM. Student's two-tailed *t* test was done to compare two groups. One-way analysis of variance (ANOVA) was used to compare multiple groups. $P > 0.05$ was considered not significant (n.s.); $P < 0.05$ was considered significant. *$P < 0.05$; **$P < 0.01$; ***$P < 0.001$; ****$P < 0.0001$.

SUPPLEMENTARY MATERIALS

immunology.sciencemag.org/cgi/content/full/6/61/eabi7083/DC1
Materials and Methods
Figs. S1 to S26
Tables S1 to S8
References (*54*–*66*)

View/request a protocol for this paper from *Bio-protocol*.

REFERENCES AND NOTES

1. M. A. Postow, R. Sidlow, M. D. Hellmann, Adverse events associated with immune checkpoint blockade. *N. Engl. J. Med.* **378**, 1165 (2018).
2. K. E. Pauken, M. Dougan, N. R. Rose, A. H. Lichtman, A. H. Sharpe, Adverse events following cancer immunotherapy: Obstacles and opportunities. *Trends Immunol.* **40**, 511–523 (2019).
3. H. Abu-Sbeih, D. M. Faleck, B. Ricciuti, R. B. Mendelsohn, A. R. Naqash, J. V. Cohen, M. C. Sellers, A. Balaji, G. Ben-Betzalel, I. Hajir, J. Zhang, M. M. Awad, G. C. Leonardi, D. B. Johnson, D. J. Pinato, D. H. Owen, S. A. Weiss, G. Lamberti, M. P. Lythgoe, L. Manuzzi, C. Arnold, W. Qiao, J. Naidoo, G. Markel, N. Powell, S. J. Yeung, E. Sharon, M. Dougan, Y. Wang, Immune checkpoint inhibitor therapy in patients with preexisting inflammatory bowel disease. *J. Clin. Oncol.* **38**, 576–583 (2020).
4. K. Haratani, H. Hayashi, Y. Chiba, K. Kudo, K. Yonesaka, R. Kato, H. Kaneda, Y. Hasegawa, K. Tanaka, M. Takeda, K. Nakagawa, Association of immune-related adverse events with nivolumab efficacy in non–small-cell lung cancer. *JAMA Oncol.* **4**, 374–378 (2018).
5. V. Shankaran, H. Ikeda, A. T. Bruce, J. M. White, P. E. Swanson, L. J. Old, R. D. Schreiber, IFNγ and lymphocytes prevent primary tumour development and shape tumour immunogenicity. *Nature* **410**, 1107–1111 (2001).
6. M. L. Broz, M. Binnewies, B. Boldajipour, A. E. Nelson, J. L. Pollack, D. J. Erle, A. Barczak, M. D. Rosenblum, A. Daud, D. L. Barber, S. Amigorena, L. J. Van't Veer, A. I. Sperling, D. M. Wolf, M. F. Krummel, Dissecting the tumor myeloid compartment reveals rare activating antigen-presenting cells critical for t cell immunity. *Cancer Cell* **26**, 638–652 (2014).
7. C. S. Garris, S. P. Arlauckas, R. H. Kohler, M. P. Trefny, S. Garren, C. Piot, C. Engblom, C. Pfirschke, M. Siwicki, J. Gungabeesoon, G. J. Freeman, S. E. Warren, S. Ong, E. Browning, C. G. Twitty, R. H. Pierce, M. H. Le, A. P. Algazi, A. I. Daud, S. I. Pai, A. Zippelius, R. Weissleder, M. J. Pittet, Successful anti-PD-1 cancer immunotherapy requires T cell-dendritic cell crosstalk involving the cytokines IFN-γ and IL-12. *Immunity* **49**, 1148–1161.e7 (2018).
8. B. Maier, A. M. Leader, S. T. Chen, N. Tung, C. Chang, J. LeBerichel, A. Chudnovskiy, S. Maskey, L. Walker, J. P. Finnigan, M. E. Kirkling, B. Reizis, S. Ghosh, N. R. D'Amore, N. Bhardwaj, C. V. Rothlin, A. Wolf, R. Flores, T. Marron, A. H. Rahman, E. Kenigsberg, B. D. Brown, M. Merad, A conserved dendritic-cell regulatory program limits antitumour immunity. *Nature* **580**, 257–262 (2020).
9. S. K. Greaney, A. P. Algazi, K. K. Tsai, K. T. Takamura, L. Chen, C. G. Twitty, L. Zhang, A. Paciorek, R. H. Pierce, M. H. Le, A. I. Daud, L. Fong, Intratumoral plasmid IL12 electroporation therapy in patients with advanced melanoma induces systemic and intratumoral t-cell responses. *Cancer Immunol. Res.* **8**, 246–254 (2020).
10. C. S. Grasso, J. Tsoi, M. Onyshchenko, G. Abril-Rodriguez, P. Ross-Macdonald, M. Wind-Rotolo, A. Champhekar, E. Medina, D. Y. Torrejon, D. S. Shin, P. Tran, Y. J. Kim, C. Puig-Saus, K. Campbell, A. Vega-Crespo, M. Quist, C. Martignier, J. J. Luke, J. D. Wolchok, D. B. Johnson, B. Chmielowski, F. S. Hodi, S. Bhatia, W. Sharfman, W. J. Urba, C. L. Slingluff, A. Diab, J. B. A. G. Haanen, S. M. Algarra, D. M. Pardoll, V. Anagnostou, S. L. Topalian, V. E. Velculescu, D. E. Speiser, A. Kalbasi, A. Ribas, Conserved interferon-γ signaling drives clinical response to immune checkpoint blockade therapy in melanoma. *Cancer Cell* **38**, 500 (2020).
11. E. A. Chiocca, J. S. Yu, R. V. Lukas, I. H. Solomon, K. L. Ligon, H. Nakashima, D. A. Triggs, D. A. Reardon, P. Wen, B. M. Stopa, A. Naik, J. Rudnick, J. L. Hu, P. Kumthekar, B. Yamini, J. Y. Buck, N. Demars, J. A. Barrett, A. B. Gelb, J. Zhou, F. Lebel, L. J. N. Cooper, Regulatable interleukin-12 gene therapy in patients with recurrent high-grade glioma: Results of a phase 1 trial. *Sci. Transl. Med.* **11**, eaaw5680 (2019).
12. B. D. Car, V. M. Eng, J. M. Lipman, T. D. Anderson, The toxicology of interleukin-12: A review. *Toxicol. Pathol.* **27**, 58–63 (1999).
13. W. Lasek, R. Zagożdżon, M. Jakobisiak, Interleukin 12: Still a promising candidate for tumor immunotherapy? *Cancer Immunol. Immunother.* **63**, 419–435 (2014).
14. C. Bonnans, G. Thomas, W. He, B. Jung, W. Chen, M. Liao, J. Heyen, B. Buetow, S. Pillai, D. Matsumoto, J. Chaparro-Riggers, S. Salek-Ardakani, Y. Qu, CD40 agonist-induced IL-12p40 potentiates hepatotoxicity. *J. Immunother. Cancer* **8**, 10.1136/jitc-2020-000624, (2020).
15. A. M. Luoma, S. Suo, H. L. Williams, T. Sharova, K. Sullivan, M. Manos, P. Bowling, F. S. Hodi, O. Rahma, R. J. Sullivan, G. M. Boland, J. A. Nowak, S. K. Dougan, M. Dougan, G. C. Yuan, K. W. Wucherpfennig, Molecular pathways of colon inflammation induced by cancer immunotherapy. *Cell* **182**, 655–671.e22 (2020).
16. P. Johnson, R. Challis, F. Chowdhury, Y. Gao, M. Harvey, T. Geldart, P. Kerr, C. Chan, A. Smith, N. Steven, C. Edwards, M. Ashton-Key, E. Hodges, A. Tutt, C. Ottensmeier, M. Glennie, A. Williams, Clinical and biological effects of an agonist anti-CD40 antibody: A cancer research UK phase I study. *Clin. Cancer Res.* **21**, 1321–1328 (2015).
17. S. P. Arlauckas, C. S. Garris, R. H. Kohler, M. Kitaoka, M. F. Cuccarese, K. S. Yang, M. A. Miller, J. C. Carlson, G. J. Freeman, R. M. Anthony, R. Weissleder, M. J. Pittet, In vivo imaging reveals a tumor-associated macrophage-mediated resistance pathway in anti-PD-1 therapy. *Sci. Transl. Med.* **9**, eaal3604 (2017).
18. S. Hoves, C. H. Ooi, C. Wolter, H. Sade, S. Bissinger, M. Schmittnaegel, O. Ast, A. M. Giusti, K. Wartha, V. Runza, W. Xu, Y. Kienast, M. A. Cannarile, H. Levitsky, S. Romagnoli, M. De Palma, D. Rüttinger, C. H. Ries, Rapid activation of tumor-associated macrophages boosts preexisting tumor immunity. *J. Exp. Med.* **215**, 859–876 (2018).
19. G. L. Beatty, D. A. Torigian, E. G. Chiorean, B. Saboury, A. Brothers, A. Alavi, A. B. Troxel, W. Sun, U. R. Teitelbaum, R. H. Vonderheide, P. J. O'Dwyer, A phase I study of an agonist CD40 monoclonal antibody (CP-870,893) in combination with gemcitabine in patients with advanced pancreatic ductal adenocarcinoma. *Clin. Cancer Res.* **19**, 6286–6295 (2013).
20. J. P. Leonard, M. L. Sherman, G. L. Fisher, L. J. Buchanan, G. Larsen, M. B. Atkins, J. A. Sosman, J. P. Dutcher, N. J. Vogelzang, J. L. Ryan, Effects of single-dose interleukin-12 exposure on interleukin-12-associated toxicity and interferon-gamma production. *Blood* **90**, 2541–2548 (1997).
21. J. E. Portielje, W. H. Kruit, M. Schuler, J. Beck, C. H. Lamers, G. Stoter, C. Huber, M. de Boer-Dennert, A. Rakhit, R. L. Bolhuis, W. E. Aulitzky, Phase I study of subcutaneously administered recombinant human interleukin 12 in patients with advanced renal cell cancer. *Clin. Cancer Res.* **5**, 3983–3989 (1999).
22. C. J. Horras, C. L. Lamb, K. A. Mitchell, Regulation of hepatocyte fate by interferon-γ. *Cytokine Growth Factor Rev.* **22**, 35–43 (2011).
23. S. Spranger, D. Dai, B. Horton, T. F. Gajewski, Tumor-residing Batf3 dendritic cells are required for effector T Cell trafficking and adoptive T Cell therapy. *Cancer Cell* **31**, 711–723.e4 (2017).
24. A. H. Morrison, M. S. Diamond, C. A. Hay, K. T. Byrne, R. H. Vonderheide, Sufficiency of CD40 activation and immune checkpoint blockade for T cell priming and tumor immunity. *Proc. Natl. Acad. Sci. U.S.A.* **117**, 8022–8031 (2020).
25. T. Oba, M. D. Long, T. Keler, H. C. Marsh, H. Minderman, S. I. Abrams, S. Liu, F. Ito, Overcoming primary and acquired resistance to anti-PD-L1 therapy by induction and activation of tumor-residing cDC1s. *Nat. Commun.* **11**, 5415 (2020).
26. R. Zilionis, C. Engblom, C. Pfirschke, V. Savova, D. Zemmour, H. D. Saatcioglu, I. Krishnan, G. Maroni, C. V. Meyerovitz, C. M. Kerwin, S. Choi, W. G. Richards, A. De Rienzo, D. G. Tenen, R. Bueno, E. Levantini, M. J. Pittet, A. M. Klein, Single-cell transcriptomics of human and mouse lung cancers reveals conserved myeloid populations across individuals and species. *Immunity* **50**, 1317–1334.e10 (2019).
27. G. M. Gerhard, R. Bill, M. Messemaker, A. M. Klein, M. J. Pittet, Tumor-infiltrating dendritic cell states are conserved across solid human cancers. *J. Exp. Med.* **218**, e20200264 (2021).
28. S. Cheng, Z. Li, R. Gao, B. Xing, Y. Gao, Y. Yang, S. Qin, L. Zhang, H. Ouyang, P. Du, L. Jiang, B. Zhang, Y. Yang, X. Wang, X. Ren, J. X. Bei, X. Hu, Z. Bu, J. Ji, Z. Zhang, A pan-cancer single-cell transcriptional atlas of tumor infiltrating myeloid cells. *Cell* **184**, 792–809.e23 (2021).
29. M. M. Meredith, K. Liu, G. Darrasse-Jeze, A. O. Kamphorst, H. A. Schreiber, P. Guermonprez, J. Idoyaga, C. Cheong, K. H. Yao, R. E. Niec, M. C. Nussenzweig, Expression of the zinc finger transcription factor zDC (Zbtb46, Btbd4) defines the classical dendritic cell lineage. *J. Exp. Med.* **209**, 1153–1165 (2012).
30. M. Sakai, T. D. Troutman, J. S. Seidman, Z. Ouyang, N. J. Spann, Y. Abe, K. M. Ego, C. M. Bruni, Z. Deng, J. C. M. Schlachetzki, A. Nott, H. Bennett, J. Chang, B. T. Vu, M. P. Pasillas, V. M. Link, L. Texari, S. Heinz, B. M. Thompson, J. G. McDonald, F. Geissmann, C. K. Glass, Liver-derived signals sequentially reprogram myeloid enhancers to initiate and maintain kupffer cell identity. *Immunity* **51**, 655–670.e8 (2019).
31. I. Theurl, I. Hilgendorf, M. Nairz, P. Tymoszuk, D. Haschka, M. Asshoff, S. He, L. M. Gerhardt, T. A. Holderried, M. Seifert, S. Sopper, A. M. Fenn, A. Anzai, S. Rattik, C. McAlpine, M. Theurl, P. Wieghofer, Y. Iwamoto, G. F. Weber, N. K. Harder, B. G. Chousterman,

T. L. Arvedson, M. McKee, F. Wang, O. M. Lutz, E. Rezoagli, J. L. Babitt, L. Berra, M. Prinz, M. Nahrendorf, G. Weiss, R. Weissleder, H. Y. Lin, F. K. Swirski, On-demand erythrocyte disposal and iron recycling requires transient macrophages in the liver. *Nat. Med.* **22**, 945–951 (2016).
32. J. P. Böttcher, C. Reis e Sousa, The role of type 1 conventional dendritic cells in cancer immunity. *Trends Cancer* **4**, 784–792 (2018).
33. F. Li, J. V. Ravetch, Inhibitory Fcγ receptor engagement drives adjuvant and anti-tumor activities of agonistic CD40 Antibodies. *Science* **333**, 1030–1034 (2011).
34. C. Engblom, C. Pfirschke, M. J. Pittet, The role of myeloid cells in cancer therapies. *Nat. Rev. Cancer* **16**, 447–462 (2016).
35. K. Ley, H. M. Hoffman, P. Kubes, M. A. Cassatella, A. Zychlinsky, C. C. Hedrick, S. D. Catz, Neutrophils: New insights and open questions. *Sci Immunol.* **3**, eaat4579 (2018).
36. G. Boivin, J. Faget, P. B. Ancey, A. Gkasti, J. Mussard, C. Engblom, C. Pfirschke, C. Contat, J. Pascual, J. Vazquez, N. Bendriss-Vermare, C. Caux, M. C. Vozenin, M. J. Pittet, M. Gunzer, E. Meylan, Durable and controlled depletion of neutrophils in mice. *Nat. Commun.* **11**, 2762 (2020).
37. J. X. Wang, A. M. Bair, S. L. King, R. Shnayder, Y. F. Huang, C. C. Shieh, R. J. Soberman, R. C. Fuhlbrigge, P. A. Nigrovic, Ly6G ligation blocks recruitment of neutrophils via a β2-integrin–dependent mechanism. *Blood* **120**, 1489–1498 (2012).
38. K. D. Carr, A. N. Sieve, M. Indramohan, T. J. Break, S. Lee, R. E. Berg, Specific depletion reveals a novel role for neutrophil-mediated protection in the liver during Listeria monocytogenes infection. *Eur. J. Immunol.* **41**, 2666–2676 (2011).
39. F. Liu, H. Y. Wu, R. Wesselschmidt, T. Kornaga, D. C. Link, Impaired production and increased apoptosis of neutrophils in granulocyte colony-stimulating factor receptor–deficient mice. *Immunity* **5**, 491–501 (1996).
40. K. T. Byrne, N. H. Leisenring, D. L. Bajor, R. H. Vonderheide, CSF-1R–dependent lethal hepatotoxicity when agonistic CD40 antibody is given before but not after chemotherapy. *J. Immunol.* **197**, 179–187 (2016).
41. G. Ingoglia, A. Yalamanoglu, M. Pfefferlé, I. L. Dubach, C. A. Schaer, K. Valkova, K. Hansen, N. Schulthess, R. Humar, D. J. Schaer, F. Vallelian, Line-selective macrophage activation with an anti-CD40 antibody drives a hemophagocytic syndrome in mice. *Blood Adv.* **4**, 2751–2761 (2020).
42. X. Hou, X. Hao, M. Zheng, C. Xu, J. Wang, R. Zhou, Z. Tian, CD205-TLR9-IL-12 axis contributes to CpG-induced oversensitive liver injury in HBsAg transgenic mice by promoting the interaction of NKT cells with Kupffer cells. *Cell. Mol. Immunol.* **14**, 675–684 (2017).
43. L. Yong, M. Li, Y. Gao, Y. Deng, W. Liu, D. Huang, C. Ren, M. Liu, J. Shen, X. Hou, Identification of pro-inflammatory CD205+ macrophages in livers of hepatitis B virus transgenic mice and patients with chronic hepatitis B. *Sci. Rep.* **7**, 46765 (2017).
44. V. Shahabi, D. Berman, S. D. Chasalow, L. Wang, Z. Tsuchihashi, B. Hu, L. Panting, M. Jure-Kunkel, R. R. Ji, Gene expression profiling of whole blood in ipilimumab-treated patients for identification of potential biomarkers of immune-related gastrointestinal adverse events. *J. Transl. Med.* **11**, 75 (2013).
45. R. Matsukane, H. Watanabe, H. Minami, K. Hata, K. Suetsugu, T. Tsuji, S. Masuda, I. Okamoto, T. Nakagawa, T. Ito, M. Eto, M. Mori, Y. Nakanishi, N. Egashira, Continuous monitoring of neutrophils to lymphocytes ratio for estimating the onset, severity, and subsequent prognosis of immune related adverse events. *Sci. Rep.* **11**, 1324 (2021).
46. T. Németh, M. Sperandio, A. Mócsai, Neutrophils as emerging therapeutic targets. *Nat. Rev. Drug Discov.* **19**, 253–275 (2020).
47. S. Jaillon, A. Ponzetta, D. Di Mitri, A. Santoni, R. Bonecchi, A. Mantovani, Neutrophil diversity and plasticity in tumour progression and therapy. *Nat. Rev. Cancer* **20**, 485–503 (2020).
48. L. Meunier, D. Larrey, Chemotherapy-associated steatohepatitis. *Ann. Hepatol.* **19**, 597–601 (2020).
49. R. Zilionis, J. Nainys, A. Veres, V. Savova, D. Zemmour, A. M. Klein, L. Mazutis, Single-cell barcoding and sequencing using droplet microfluidics. *Nat. Protoc.* **12**, 44–73 (2017).
50. F. E. Mercier, D. B. Sykes, D. T. Scadden, Single targeted exon mutation creates a true congenic mouse for competitive hematopoietic stem cell transplantation: The C57BL/6-CD45.1 STEM mouse. *Stem Cell Rep.* **6**, 985–992 (2016).
51. M. Ashburner, C. A. Ball, J. A. Blake, D. Botstein, H. Butler, J. M. Cherry, A. P. Davis, K. Dolinski, S. S. Dwight, J. T. Eppig, M. A. Harris, D. P. Hill, L. Issel-Tarver, A. Kasarskis, S. Lewis, J. C. Matese, J. E. Richardson, M. Ringwald, G. M. Rubin, G. Sherlock, Gene ontology: Tool for the unification of biology. *Nat. Genet* **25**, 25–29 (2000).
52. The Gene Ontology Consortium, The gene ontology resource: 20 years and still Going strong. *Nucleic Acids Res.* **47**, D330–D338 (2019).
53. H. Mi, A. Muruganujan, D. Ebert, X. Huang, P. D. Thomas, PANTHER version 14: More genomes, a new PANTHER GO-slim and improvements in enrichment analysis tools. *Nucleic Acids Res.* **47**, D419–D426 (2019).
54. G. La Manno, R. Soldatov, A. Zeisel, E. Braun, H. Hochgerner, V. Petukhov, K. Lidschreiber, M. E. Kastriti, P. Lönnerberg, A. Furlan, J. Fan, L. E. Borm, Z. Liu, D. van Bruggen, J. Guo, X. He, R. Barker, E. Sundström, G. Castelo-Branco, P. Cramer, I. Adameyko, S. Linnarsson, P. V. Kharchenko, RNA velocity of single cells. *Nature* **560**, 494–498 (2018).
55. J. T. Robinson, H. Thorvaldsdóttir, W. Winckler, M. Guttman, E. S. Lander, G. Getz, J. P. Mesirov, Integrative genomics viewer. *Nat. Biotechnol.* **29**, 24–26 (2011).
56. A. Dobin, C. A. Davis, F. Schlesinger, J. Drenkow, C. Zaleski, S. Jha, P. Batut, M. Chaisson, T. R. Gingeras, STAR: Ultrafast universal RNA-seq aligner. *Bioinformatics* **29**, 15–21 (2013).
57. A. M. Klein, L. Mazutis, I. Akartuna, N. Tallapragada, A. Veres, V. Li, L. Peshkin, D. A. Weitz, M. W. Kirschner, Droplet barcoding for single-cell transcriptomics applied to embryonic stem cells. *Cell* **161**, 1187–1201 (2015).
58. S. L. Wolock, R. Lopez, A. M. Klein, Scrublet: Computational identification of cell doublets in single-cell transcriptomic data. *Cell Syst.* **8**, 281–291.e9 (2019).
59. F. A. Wolf, P. Angerer, F. J. Theis, SCANPY: Large-scale single-cell gene expression data analysis. *Genome Biol.* **19**, 15 (2018).
60. C. Weinreb, S. Wolock, A. M. Klein, SPRING: A kinetic interface for visualizing high dimensional single-cell expression data. *Bioinformatics* **34**, 1246–1248 (2018).
61. F. García-Alcalde, K. Okonechnikov, J. Carbonell, L. M. Cruz, S. Götz, S. Tarazona, J. Dopazo, T. F. Meyer, A. Conesa, Qualimap: Evaluating next-generation sequencing alignment data. *Bioinformatics* **28**, 2678–2679 (2012).
62. Y. Liao, G. K. Smyth, W. Shi, featureCounts: An efficient general purpose program for assigning sequence reads to genomic features. *Bioinformatics* **30**, 923–930 (2014).
63. R. Patro, G. Duggal, C. Kingsford, Salmon: Accurate, versatile and ultrafast quantification from RNA-seq data using lightweight-alignment. *BioRxiv* 10.1101/021592 , (2015).
64. M. I. Love, W. Huber, S. Anders, Moderated estimation of fold change and dispersion for RNA-seq data with DESeq2. *Genome Biol.* **15**, 550 (2014).
65. C. Soneson, M. I. Love, M. D. Robinson, Differential analyses for RNA-seq: Transcript-level estimates improve gene-level inferences. *F1000Res.* **4**, 1521 (2015).
66. J. B. A. G. Haanen, F. Carbonnel, C. Robert, K. M. Kerr, S. Peters, J. Larkin, K. Jordan, G. C. ESMO, Management of toxicities from immunotherapy: ESMO clinical practice guidelines for diagnosis, treatment and follow-up. *Ann. Oncol.* **29**, iv264–iv266 (2018).

Acknowledgments: We thank the Harvard Stem Cell Institute for help with FACS; the Single Cell Core Facility at Harvard Medical School for help with scRNA-seq experiments; the Bauer Core Facility for sequencing; A. Ciulla and the Biopolymers Facility Next-Gen Sequencing Core Facility at Harvard Medical School for expertise and instrument availability that supported this work; J. Hutchinson and the Harvard Chan Bioinformatics Core for analysis of bulk RNA-seq data; the MGH Histopathology Research Core for processing and preparation of mouse histological tissue specimens; G. J. Freeman for generously providing the anti-PD-1 antibody reagent; R. M. Locksley and H.-E. Lian for providing the IL-12p40–IRES–EYFP transgene sequence; A. H. Sharpe, F. K. Swirski, R. Nowarski, and Pittet, Klein, Weissleder, and Jain laboratory members for helpful discussions. **Funding:** This work was supported in part by the ISREC Foundation, the Robert Wenner Award from the Swiss Cancer League, the Samana Cay MGH Research Scholar Fund, NIH grants R01-AI084880 and R01-AI123349 (to M.J.P.), NIH grant R01-CA218579 (to A.M.K. and M.J.P.), NIH grant R01-CA206890 (to M.J.P. and R.W.), NIH grants R33-CA202064 and U01CA206997 (to R.W.), NIH grants R35-CA197743, U01-CA224348, and R01-CA208205 (to R.K.J.), and by Harvard Ludwig Cancer Center. M.S. and J.G. were supported in part by Landry Cancer Biology Research Fellowships. C.Pfirschke was supported in part by the MGH ECOR Tosteson Postdoctoral Fellowship. R.Z. was supported in part by the European Regional Development Fund (project no. 01.2.2-LMT-K-718-04-0002) under grant agreement with the Research Council of Lithuania. R.B. was funded by a Postdoc.Mobility Fellowship of the Swiss National Science Foundation (SNSF; P400PM_183852). A.E.Z. was supported by NIGMS T32GM007753. J.E.M. was supported in part by a National Institutes of Health Ruth L. Kirschstein National Research Service Award Individual Predoctoral Fellowship (F31HL147364). **Author contributions:** M.S. and M.J.P. initiated the study, prepared the figures, and wrote the manuscript. M.S., R.B., J.G., C.E., C.G., G.M.G., A.K., Y.L., A.E.Z., C.C., E.B., C.Pfirschke, Y.-J. L., C.Piot, and J.E.M. performed mouse experiments and related analyses. N.A.G.-F., M.M., and R.Z. performed computational analyses. A.M.K. supervised the bioinformatics analyses. C.d.V., T.K., D.M., A.C., A.W., M.F., C.S., P.-Y.D., and O.M. obtained human liver tissue and performed related experiments and analyses. Y.I. performed mouse immunohistochemistry. R.H.K. performed liver whole-mount imaging microscopy. M.M.-K. consulted on analysis of liver histological sections. S.I.P. supported experiments with the TC-1 tumor model. N.T., R.K.J., and R.W. provided input for research design and interpretation and edited the manuscript. M.J.P. supervised the study. **Competing interests:** M.J.P. has served as consultant for Aileron Therapeutics, AstraZeneca, Cygnal Therapeutics, Elstar Therapeutics, ImmuneOncia, KSQ Therapeutics, Merck, Siamab Therapeutics, and Third Rock Ventures. A.M.K. is a founder and shareholder in 1CellBio Inc. R.W. is cofounder of T2 Biosystems, Lumicell, Aikili, and Accure Health; advises Moderna, Alivio Therapeutics, and Tarveda Therapeutics; and reports personal fees from ModeRNA, Tarveda Pharmaceuticals, Lumicell, Alivio Therapeutics, and Accure Health. R.B. is shareholder of CSL Behring. M.M.-K. has served as a compensated consultant for AstraZeneca and H3 Biomedicine and received royalty from Elsevier. R.K.J. has received an Honorarium from Amgen; consultant fees from Chugai, Elpis,

Merck, Ophthotech, Pfizer, SPARC, SynDevRx, and XTuit; owns equity in Accurius, Enlight, Ophthotech, and SynDevRx; is on the Board of Trustees of Tekla Healthcare Investors, Tekla Life Sciences Investors, Tekla Healthcare Opportunities Fund, and Tekla World Healthcare Fund; and received a research grant from Boehringer Ingelheim. These commercial relationships are unrelated to the current study. **Data and materials availability:** All data needed to evaluate the conclusions in the paper are present in the paper or the Supplementary Materials. Sequencing datasets for scRNA-seq and bulk RNA-seq have been deposited to GEO with the accession nos. GSE176109 and GSE175737, respectively. The scRNA-seq data can also be viewed using the following interactive SPRING links: IL-12-EYFP$^+$ cells (Fig. 4, A to D, and fig. S9); CD45$^+$ liver cells (Fig. 6, A and B; figs. S14 and S15; Fig. 7, B and F; and figs. S19 and S21); and all cells combined.

Submitted 25 March 2021
Accepted 3 June 2021
Published 2 July 2021
10.1126/sciimmunol.abi7083

Citation: M. Siwicki, N. A. Gort-Freitas, M. Messemaker, R. Bill, J. Gungabeesoon, C. Engblom, R. Zilionis, C. Garris, G. M. Gerhard, A. Kohl, Y. Lin, A. E. Zou, C. Cianciaruso, E. Bolli, C. Pfirschke, Y.-J. Lin, C. Piot, J. E. Mindur, N. Talele, R. H. Kohler, Y. Iwamoto, M. Mino-Kenudson, S. I. Pai, C. de Vito, T. Koessler, D. Merkler, A. Coukos, A. Wicky, M. Fraga, C. Sempoux, R. K. Jain, P.-Y. Dietrich, O. Michielin, R. Weissleder, A. M. Klein, M. J. Pittet, Resident Kupffer cells and neutrophils drive liver toxicity in cancer immunotherapy. *Sci. Immunol.* **6**, eabi7083 (2021).

Science Immunology

Resident Kupffer cells and neutrophils drive liver toxicity in cancer immunotherapy

Marie Siwicki, Nicolas A. Gort-Freitas, Marius Messemaker, Ruben Bill, Jeremy Gungabeesoon, Camilla Engblom, Rapolas Zilionis, Christopher Garris, Genevieve M. Gerhard, Anna Kohl, Yunkang Lin, Angela E. Zou, Chiara Cianciaruso, Evangelia Bolli, Christina Pfirschke, Yi-Jang Lin, Cecile Piot, John E. Mindur, Nilesh Talele, Rainer H. Kohler, Yoshiko Iwamoto, Mari Mino-Kenudson, Sara I. Pai, Claudio deVito, Thibaud Koessler, Doron Merkler, Alexander Coukos, Alexandre Wicky, Montserrat Fraga, Christine Sempoux, Rakesh K. Jain, Pierre-Yves Dietrich, Olivier Michielin, Ralph Weissleder, Allon M. Klein and Mikael J. Pittet

Sci. Immunol. **6**, eabi7083.
DOI: 10.1126/sciimmunol.abi7083

Distinction between toxicity and antitumor effects

Immune checkpoint blockade (ICB) has revolutionized cancer therapeutics; however, in many cases, ICB is limited by immune-related adverse events (irAEs). Thus, a better understanding of the immune responses that lead to irAEs and how they are distinguished from antitumor immunity is needed. Here, Siwicki *et al.* used anti-CD40 therapy as a mediator of T_H1-induced antitumor immunity in mouse tumor models. They found that liver-resident Kupffer cells induced neutrophil-mediated liver toxicity by producing IL-12 and responding to IFN-γ. Inhibition of the neutrophil response limited liver toxicity while retaining the antitumor efficacy of anti-CD40. Similar data were found in patients treated with anti–PD-1 and anti–CTLA-4. Together, these data suggest that the toxicity of ICB can be inhibited without negatively affecting antitumor immunity.